Acta Materialia 233 (2022) 117989

Contents lists available at ScienceDirect

Acta Materialia

journal homepage: www.elsevier.com/locate/actamat

Full length article

Critical stress prediction upon accurate dislocation core description

Ahmed Sameer Khan Mohammed[1], Orcun Koray Celebi[1], Huseyin Sehitoglu*

Department of Mechanical Science and Engineering, University of Illinois at Urbana-Champaign, 105 S. Mathews Ave., Urbana, IL 61801, USA

ARTICLE INFO

Article history:
Received 14 March 2022
Revised 28 April 2022
Accepted 29 April 2022
Available online 3 May 2022

Keywords:
Dislocations
Core width
Critical stress
Peierls
Stacking fault

ABSTRACT

Existing approaches for friction (critical) stress determination are highly unsatisfactory because of empiricism associated with determination of dislocation "core-width" and nature of core-advance. This study, focusing on the $^{a}/_{2}\langle 011\rangle$ extended-dislocation (partials bounding a stacking-fault) in Face-Centered-Cubic (FCC) materials, rigorously derives the core-width with continuum strain-energy and atomistic misfit-energy considerations. The strain-energy is calculated using the fully-anisotropic Eshelby-Stroh formalism accommodating the inherent mixed characters of the $^{a}/_{6}\langle 112\rangle$ Shockley-partials constituting pure-edge/pure-screw $^{a}/_{2}\langle 011\rangle$ dislocations. The misfit-energy is determined from critical fault-energies of the slip-plane input to a novel misfit-model capturing the lattice structure of the slip-plane and involving the discrete Wigner-Seitz cell area at each lattice site, advancing over an 80-year old misfit-energy model that has missed the role of both concepts. For the first time in literature, the nature of motion of the $^{a}/_{2}\langle 011\rangle$ extended-dislocation's core is rigorously derived from an optimized trajectory of its total-energy. It is shown that each $^{a}/_{6}\langle 112\rangle$ partial's core moves intermittently ("zig-zag" motion), and not together, allowing the stacking-fault width to fluctuate during advance of the extended-dislocation. The critical stress is shown to involve a trajectory-dependent combination of Schmid factors for each Shockley-partial, also revealed for the first time. The proposed model is used to predict critical stress for multiple FCC materials, including a high-entropy alloy (HEA), displaying excellent agreement with experiments. The work opens future avenues for rapid reliable assessment of a multitude of compositions across varying lattice structures (e.g. hexagonal lattices), advancing over prior exponential models for critical stress which can produce errors as high as two orders of magnitude.

1. Introduction

One of the most important mechanical properties in structural materials is the yield strength, notable as the first point of slope change in the stress-strain curve of the material. At this point, the sustained deformation of the material transitions from a recoverable/elastic nature to an irrecoverable/inelastic nature. This inelasticity is associated with an operative underlying mechanism causing microstructural changes. The predominant mechanism in crystalline structural materials is the motion/"slip" of intrinsic defects in the crystal structure known as dislocations. Thus, the yield strength of the material is dictated by the Critical Resolved Shear Stress (CRSS) on the slip system of the dislocation required for the onset of dislocation slip. A fully predictive model for this CRSS, consistent with experimental measurements, is yet to emerge precluding reliable prediction of the yield strength. The advent of such a predictive model is vital for informed exploration of the compositional design space for next-generation structural and functional alloys [1–8]. This study proposes such a model for the CRSS involving no empirical parameters.

1.1. Core structure fundamentals: disregistry and dislocation density distributions

The CRSS is determined from the intrinsic lattice resistance or lattice friction to be overcome for dislocation motion. The lattice resistance is associated with atomic-scale restoring forces operating across the slip plane of the dislocation. And in order to quantify this resistance, a clear understanding of the dislocation core is required. The Peierls model of the dislocation is adopted for this purpose. This model of the dislocation core is presented here briefly, and the reader is referred to [9–11] for a detailed exposition. A dislocation introduces a "disregistry" in the crystal structure where one half-space of the crystal structure is relatively displaced as compared to the other half-space. Both half-spaces are separated by the slip plane on which the dislocation resides, and the relative displacement introduced is given by the Burgers vector of the dislocation. This is illustrated with the help of the schematic in Fig. 1(a, b). In the global coordinate system $x_1 - x_2 - x_3$, consider

* Corresponding author.
E-mail address: huseyin@illinois.edu (H. Sehitoglu).
[1] Both authors contributed equally to this paper

https://doi.org/10.1016/j.actamat.2022.117989
1359-6454/

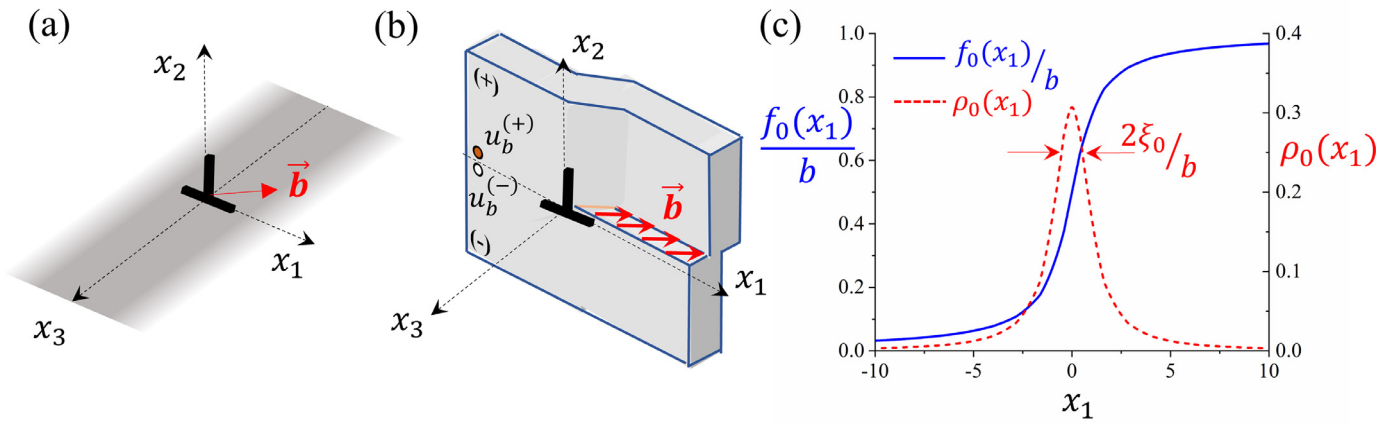

Fig. 1. Dislocation core-structure: (a) the $x_1 - x_2 - x_3$ coordinate system attached to a dislocation with Burgers vector $\vec{b}$, the dislocation line aligned with x_3 axis and the slip plane as the $x_1 - x_2$ plane; (b) a three-dimensional visualization of the disregistry distribution across the slip plane, indicating the (+) and (-) half-spaces and displacement components $u_b^{(\pm)}(x_1)$ alluded to in the main text and (c) plots of the disregistry distribution $f_0(x_1) = u_b^{(+)}(x_1) - u_b^{(-)}(x_1)$ and its derivative $\rho_0(x_1)$, representing the dislocation core-width ξ (defined in Eq. (1)).

the dislocation line to be perfectly straight and aligned with the x_3 axis and the normal to the slip plane be given by unit vector $\hat{e}_2$ along x_2 axis. In the $x_1 - x_2$ plane, the dislocation is positioned at $(0, 0)$. Now, consider the two half-spaces of the material separated by the slip plane i.e. the $x_1 - x_3$ plane. Denote the top half-space, where $x_2 > 0$, to be the (+) half space and the bottom half-space, where $x_2 < 0$, to be the (-) half-space. Consider the displacement field introduced by the dislocation to be given by $u_i(x_1, x_2)$, where $i = 1, 2, 3$. This displacement field does not vary along the dislocation line and is hence independent of x_3. Consider the displacement of the (+) half-space taken at the slip plane. This is given by $u_i^{(+)}(x_1) = \lim_{x_2 \to 0^+} u_i(x_1, x_2)$, and for the bottom half-space we can respectively define the displacement $u_i^{(-)}(x_1) = \lim_{x_2 \to 0^-} u_i(x_1, x_2)$. Resolve the displacement along the direction of the Burgers vectors, yielding the scalar components $u_b^{(\pm)}(x_1) = u_i^{(\pm)}(x_1).{}^{b_i}/_b$, where $\vec{b} = b_i \hat{e}_i$ represents the Burgers vector of the dislocation with magnitude b and the Einstein summation convention is utilized in the equation. The disregistry distribution $f(x_1)$ can now be defined as the relative displacement along the Burgers vector at the slip-plane given by $f(x_1) = u_b^{(+)}(x_1) - u_b^{(-)}(x_1)$. In the Peierls model of the dislocation, this disregistry-distribution is solved for from an integro-differential equation. This equation considers the balance of elastic forces resulting from the strain-field of the dislocation and the restoring atomistic force exerted by the lattice sustaining this displacement-field at the slip plane. Consequently, the disregistry distribution is given by

$$f_0(x_1) = \frac{b}{2} + \frac{b}{\pi} \tan^{-1}\left(\frac{x_1}{\xi_0}\right) \tag{1}$$

where b is the magnitude of the Burgers vector of the dislocation and ξ_0 is defined as the "core-width" of the dislocation. The core-width is better represented by the dislocation density distribution $\rho_0(x_1)$ which is the derivative of the disregistry distribution. It is given by the equation

$$\rho_0(x_1) = \frac{b}{\pi}\left(\frac{\xi_0}{{x_1}^2 + \xi_0^2}\right) \tag{2}$$

plotted in Fig. 1(c). It is this core-width that strongly dictates the CRSS. Multiple approaches to predict this core-width have been proposed in literature [9,11–42]. However, they are challenged by multiple limitations that have precluded a reliable prediction for the CRSS, as discussed in the following section. This study addresses all challenges to develop a robust framework for CRSS-prediction agreeing with available experimental data.

1.2. Limitations of existing approaches

In the classical formalism of the Peierls dislocation [9–11,14], the core-width was determined within assumptions of elastic isotropy, and the understanding that the atomistic restoring forces are dependent on the isotropic shear modulus μ. Extensions to account for elastic anisotropy have also been proposed in analytical approaches by way of introducing an anisotropic coefficient K or an anisotropic tensor H to calculate the expression for core-width [12,13,15–18,24,31,32,39,41,43,44]. Additional improvements were proposed to replace atomistic restoring-force law to include the ideal shear-strength on the slip system $\tau_{\max}$ instead of the modulus [16,18,31,45,46]. Further, to determine the CRSS from the core-width, analytical formulae were proposed in two limits, where either the core-width is very small ("narrow" dislocation core) or very high ("wide" dislocation core) [46]. While all of these advancements were critical to improve our understanding of the dislocation-core and the CRSS, there are existing limitations which the current study proposes to resolve. The fundamental background is listed in (a) and (b) below, and the new approach emphasized in (c)-(f):

a **Elastic anisotropy:** Crystalline materials are in general anisotropic, and their elastic constitution must be adequately accounted for without isotropic approximations. While the anisotropic coefficient K is a convenient introduction into the formalism, its determination involves some form of empiricism or underlying presumption regarding the elastic behavior surrounding the dislocation core, without direct consideration of the strain-energy itself. An unambiguous determination of the anisotropic coefficient directly from the anisotropic strain-energy of the dislocation core is required for accurate calculation of the core-width, as proposed in this study.

b **Atomistic fault energies:** Planar fault energies for the slip system must be determined and incorporated to have the correct atomistic restoring-forces in the dislocation cores. The critical aspect here is that the restoring force operative across the slip plane of the dislocation core is in response to a planar disregistry between two half-spaces and not the same as a continuum shear across the slip plane. Thus, the use of shear-modulus μ and the ideal shear strength $\tau_{\max}$ is not appropriate for the restoring-force law. For the case of FCC materials as considered

in this study, the fault energy barriers correspond to the stable intrinsic stacking fault energy γ_{isf} and the unstable stacking fault energy barrier γ_{us} on the Generalized Stacking Fault Energy (GSFE) landscape. These energy barriers can now be well-predicted using atomistic modeling tools such as Density Functional Theory (DFT) or Molecular Statics (MS), and must be incorporated.

c **Influence of parent lattice structure:** A central assumption in any existing model for critical stress lies in the calculation of the energy of misfit on the slip-plane. All existing models to date, to the best of the authors' knowledge, employ a one-dimensional series-summation for the misfit-energy which uses a discrete parameter a' corresponding to a certain interplanar spacing of the lattice (a detailed exposition is deferred to Section 2.2.2). This choice dates back to the original model by Peierls [9] from over 80 years back. Such a model does not capture the lattice-dependent distribution of the discrete atomic-positions on the slip-plane of the lattice. This study proposes a fundamental change in this misfit-energy model incorporating both the slip-plane lattice-structure and advancing the choice of a' to a more fundamental quantity known as the Wigner-Seitz cell area of the slip-plane lattice.

d **Mixed character of Shockley partials**: Although prior models have been developed to treat dislocations with mixed character [16,17,38,46,47], a robust framework suited to $a/2\langle 011\rangle$ extended dislocations is required. This is because even for a pure-edge/pure-screw character of the $a/2\langle 011\rangle$ extended dislocation, the nature of the individual $a/6\langle 112\rangle$ Shockley partials constituting the extended dislocation is always mixed. To truly predict the CRSS in this case, the predictive model must accommodate mixed dislocation character, as proposed in this study.

e **Nature of motion of extended dislocation**: In order to determine the CRSS of extended dislocations, it is important to know how each of the Shockley partials of the dislocation moves through the lattice. In this description, it is common to presume a nature of dislocation motion where both the Shockley partials are moving together simultaneously such that the fault-width between them does not change. This fundamental presumption is challenged in this study and it is shown that the Shockley partials can move intermittently or in a "zig-zag" motion where, first the leading Shockley partial moves forward with the trailing-partial unmoved and then the trailing-partial moves with the leading partial fixed. Such a motion allows for the fault-width between the partials to fluctuate as the dislocation moves and is shown to be energetically preferred.

f **Resolved Shear Stress (RSS) on $a/6\langle 112\rangle$ Shockley partials and $a/2\langle 011\rangle$ extended-dislocation:** The critical stress for dislocation motion is generally determined as the critical magnitude of the RSS on the slip-system, at which dislocation motion is initiated. And for a slip-system where the slip-plane normal is $\hat{n}$ and the direction of slip is $\hat{m}$, the resolved shear stress is given by $\tau_{RSS} = (\underline{\underline{\sigma_a}}\hat{n}).\hat{m}$, where $\underline{\underline{\sigma_a}}$ is the applied stress tensor. The slip-direction is parallel to the Burgers vector of the dislocations on the slip system and thus the same equation can be rewritten as $\tau_{RSS} = (\underline{\underline{\sigma_a}}\hat{n}).\hat{b}$, where $\hat{b}$ represents the unit vector along the direction of the Burgers vector. While the above formulation works well for single dislocations without partials or a stacking fault, it immediately poses a problem for the case of an $a/2\langle 011\rangle$ extended dislocation in FCC materials. This is because there are three Burgers vectors involved in the system, that of the two $a/6\langle 112\rangle$ Shockley partials and the $a/2\langle 011\rangle$ dislocation that these partials constitute. For a given applied stress-tensor, there are three operative RSS magnitudes corresponding to each of the three Burgers vectors and it is fundamental to know how they couple with each other in order to determine the CRSS of the FCC slip-system. This has not been addressed till date, to the best of the authors' knowledge, and will be rigorously derived in this study.

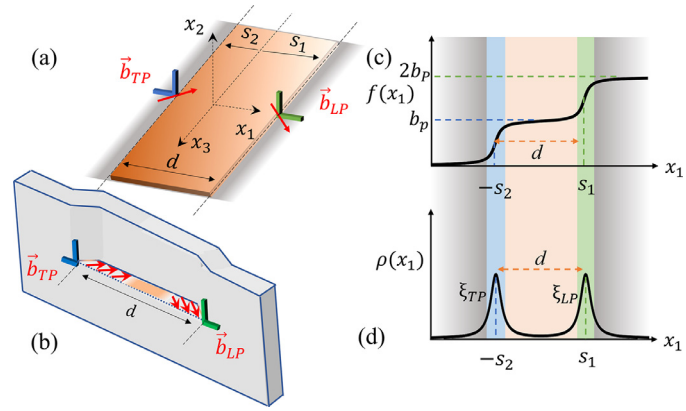

Fig. 2. Core-structure of an $a/2\langle 011\rangle$ extended dislocation in FCC materials: (a) An extended dislocation constituting a leading partial $\vec{b}_{LP}$, a trailing partial $\vec{b}_{TP}$ and, a stacking fault of width d bounded by the two partials; the $x_1 - x_2 - x_3$ coordinate system attached to the extended dislocation is given; the leading partial is at position $x_1 = s_1$ and the trailing partial is at $x_1 = -s_2$, yielding the fault-width between them as $d = s_1 + s_2$ (b) a schematic three-dimensional view of the extended dislocation is shown, indicating how the fault forms between the two partials; plots of the (c) disregistry distribution, $f(x_1)$, and (d) the dislocation-density distribution, $\rho(x_1)$, of the extended dislocation, indicating the core-widths $\xi_{TP,LP}$ of the trailing and leading partials respectively.

1.3. Current approach

The current study improves on all aforementioned fronts to develop a predictive model for the CRSS of FCC materials, without involving any empiricism. An energy-based approach is forwarded that predicts the core-width through a balance of continuum strain-energy and atomistic misfit-energy, subsequently utilized to predict the CRSS. The continuum strain-energy is determined directly from the strain-field of the dislocation, fully accounting for material anisotropy through the Eshelby-Stroh formalism. The misfit-energy is determined based on the GSFE landscape, incorporating both γ_{isf} and γ_{us} fault-energy barriers, and the structure of the slip-plane lattice into the formalism. The predicted core-width is then utilized to determine the CRSS of $a/2\langle 011\rangle$ edge and screw dislocations. The individual Shockley partials $a/6\langle 112\rangle$ are of mixed characters in both cases. The framework predicts the stacking fault width in addition to the core-widths of the Shockley partials, subsequently used to predict the CRSS, validated by comparison with experimental data. The methodology and results from the predictive framework are elaborated in the Section 2 below, presented concurrently for better clarity. The implications of the results and the proposed framework are discussed in Section 3. Section 4 concludes the study with a summary of all proposed contributions of this study.

2. Methodology and results

2.1. Core-structure of the $a/2\langle 011\rangle$ extended dislocation

The CRSS is predicted for the $\vec{b}_F = a/2[\bar{1}\bar{1}0]$ dislocation on a $(1\bar{1}1)$ plane in the FCC structure. This dislocation dissociates into two Shockley partials, a leading partial $\vec{b}_{LP} = a/6[\bar{1}\bar{2}\bar{1}]$ and a trailing partial $\vec{b}_{TP} = a/6[\bar{2}\bar{1}1]$, schematically represented in Fig. 2(a). Henceforth, any reference to the $a/2\langle 011\rangle$ extended dislocation implies reference to the dislocation $\vec{b}_F$ considered in this study, with the connotation that the proposed analytical framework applies to

all extended dislocations of the $^a/_2\langle 011\rangle$ family in FCC materials. The proposed framework is developed and illustrated for both the edge and screw character of the extended dislocation. For each character, the global coordinate systems are respectively defined as follows:

a For screw character: $\hat{e}_1||[1\bar{1}\bar{2}]$, $\hat{e}_2||[1\bar{1}1]$ and $\hat{e}_3||[\bar{1}\bar{1}0]$
b For edge character: $\hat{e}_1||[\bar{1}\bar{1}0]$, $\hat{e}_2||[1\bar{1}1]$ and $\hat{e}_3||[\bar{1}12]$

where $\hat{e}_i$ is the unit vector along the global x_i axes for $i = 1, 2, 3$. The dislocation line is chosen to be aligned with the x_3 axis. Note that even though the $^a/_2\langle 011\rangle$ extended dislocation has a pure edge/screw character, the individual Shockley partials have a general mixed character in both cases, and the proposed framework offers capabilities to model this behavior. The magnitude of the full dislocation $\vec{b}_F$ will be represented by b_F, and that of the partials will be given by b_P. The center of the leading partial's core is located at $x_1 = s_1$, while that of the trailing partial is at $x_1 = -s_2$, so that the fault-width between them is given by $d = s_1 + s_2$ (refer Fig. 2 (a, b)). The core-structure of the extended dislocation is generally given by the following disregistry distribution

$$f(x_1) = b_P + \frac{b_P}{\pi}\left(\tan^{-1}\left(\frac{x_1 + s_2}{\xi_{TP}}\right) + \tan^{-1}\left(\frac{x_1 - s_1}{\xi_{LP}}\right)\right) \tag{3}$$

The dislocation density distribution $\rho(x_1)$, calculated as the derivative of $f(x_1)$, is given by:

$$\rho(x_1) = \frac{b_P}{\pi}\left(\frac{\xi_{TP}}{(x_1 + s_2)^2 + \xi_{TP}^2} + \frac{\xi_{LP}}{(x_1 - s_1)^2 + \xi_{LP}^2}\right) \tag{4}$$

In this study, the extended form is decomposed into the core-distributions of the individual partials. This is done since the Burgers vector directions of both partials are not aligned (refer Fig. 2(a, b)) and are different vectors themselves. A separate treatment allows the approach to capture the core-energies better, particularly the strain-energies of both the cores, leading to a more accurate analysis. In that regard, the core disregistry distribution of the leading and trailing partials, and their corresponding dislocation density distributions are respectively given by the equations:

$$f_{TP}(x_1) = \frac{b_P}{2} + \frac{b_P}{\pi}\tan^{-1}\left(\frac{x_1 + s_2}{\xi_{TP}}\right)$$
$$\rho_{TP}(x_1) = \frac{b_P}{\pi}\left(\frac{\xi_{TP}}{(x_1 + s_2)^2 + \xi_{TP}^2}\right) \tag{5}$$

$$f_{LP}(x_1) = \frac{b_P}{2} + \frac{b_P}{\pi}\tan^{-1}\left(\frac{x_1 - s_1}{\xi_{LP}}\right)$$
$$\rho_{LP}(x_1) = \frac{b_P}{\pi}\left(\frac{\xi_{LP}}{(x_1 - s_1)^2 + \xi_{LP}^2}\right) \tag{6}$$

Note that the above equations are an additive decomposition of the extended form Eqs. (3) and ((4)), since $f_{TP}(x_1) + f_{LP}(x_1) = f(x_1)$ and $\rho_{TP}(x_1) + \rho_{LP}(x_1) = \rho(x_1)$. Thus, the core structure of the $^a/_2\langle 011\rangle$ extended dislocation is completely characterized by the core-width ξ_{TP} of the trailing partial, core-width ξ_{LP} of the leading partial, and the positions s_1 and s_2. These parameters are determined ab initio from an energy-minimization approach described below.

2.2. Energy of the extended dislocation: continuum-strain energy and atomistic misfit energy

The $^a/_2\langle 011\rangle$ extended dislocation has two components to its total energy, E_{TOT}: (i) strain energy due to continuum strain-fields introduced by the dislocation, E_{STRAIN}, and (ii) atomistic misfit energy at the core of the dislocation, E_{MISFIT}, due to the disregistries on its slip plane and the associated fault energy cost of the same. Both energy components depend on the parameters $(\xi_{TP}, \xi_{LP}, s_1, s_2)$. Thus we have the relation:

$$E_{TOT}(\xi_{TP}, \xi_{LP}, s_1, s_2) = E_{STRAIN}(\xi_{TP}, \xi_{LP}, s_1, s_2) + E_{MISFIT}(\xi_{TP}, \xi_{LP}, s_1, s_2) \tag{7}$$

Calculation of the individual energy components is described below.

2.2.1. Elastic strain-energy: anisotropic formalism

The continuum strain-energy $E_{STRAIN}(\xi_{TP}, \xi_{LP}, s_1, s_2)$ of the extended dislocation is determined by calculation of 3 anisotropic interaction coefficients K_{11}, K_{22}, and K_{12}, each of which respectively captures the strain-energy of self-interaction of the leading partial, strain-energy of self-interaction of the trailing-partial and the strain-energy of interaction between the two partials. These coefficients are calculated directly from the strain-energies determined from the anisotropic Eshelby-Stroh (E-S) formalism [48,49]. The methodology to determine K_{12} is elucidated first. Consider the leading Shockley partial, with Burgers vector $\vec{b}_{LP}$ and the trailing partial $\vec{b}_{TP}$, separated by a distance R as shown in Fig. 3(a). The continuum strain-fields surrounding each partial are determined from the E-S formalism and superposed to determine the net strain-field surrounding both partials. Subsequently, the strain-energy density is numerically integrated to determine the total strain-energy of interaction, $E_{\perp-\perp}(R)$ at the chosen separation distance R. In the integration of the strain-energy densities, a core-region within radius $r_0 = 5b_P$ around the center of each partial is excluded since the continuum formalism does not hold in this core-region. By calculating the strain-energy $E_{\perp-\perp}(R)$ at varying R, the interaction coefficient K_{12} is determined (Fig. 3 (a)). This choice of r_0 does not change the K_{12} calculation since irrespective of this choice, the gradient of change of $E_{\perp-\perp}(R)$ is conserved. This procedure is elaborated further below.

The E-S formalism is described briefly here and the reader is referred to [48,49] for a more detailed exposition. Following this formalism, the displacement-field for a dislocation with arbitrary Burgers vector, $\vec{b}$, can be analytically expressed in terms of certain anisotropic E-S constants, given by the equation,

$$u_i(x_1, x_2) = \frac{1}{2\pi\sqrt{-1}}\sum_{\alpha=1}^{6}\eta_\alpha A_{i\alpha}L_{s\alpha}b_s\ln(x_1 + p_\alpha x_2) \tag{8}$$

where $\eta_\alpha = 1$ for $\alpha \in \{1, 2, 3\}$ and $\eta_\alpha = -1$ for $\alpha \in \{4, 5, 6\}$, and $\{p_\alpha, A_{i\alpha}, L_{s\alpha}\}$ are the E-S constants. The E-S constants are solved for from the equations:

$$\left\|(C_{ijkm}(\delta_{i1} + p_\alpha\delta_{i2})(\delta_{m1} + p_\alpha\delta_{m2})\right\| = 0 \tag{9}$$

$$C_{ijkm}(\delta_{i1} + p_\alpha\delta_{i2})(\delta_{m1} + p_\alpha\delta_{m2})A_{k\alpha} = 0 \tag{10}$$

$$L_{j\alpha} = -\delta_{i2}C_{ijkm}(\delta_{m1} + p_\alpha\delta_{m2})A_{k\alpha} \tag{11}$$

where C_{ijkl} is the fully-anisotropic elastic-constant tensor in the $x_1 - x_2 - x_3$ coordinate system and δ_{ij} is the Kronecker delta function. The cubic elastic constants of the FCC materials considered in this study are listed in Table 1. Given the displacement-field, the strain-field is calculated using the relation,

$$\varepsilon_{ij} = \frac{1}{2}\left(\frac{\partial u_i}{\partial x_j} + \frac{\partial u_j}{\partial x_i}\right) \tag{12}$$

Substituting (8) in (12), the strain-field is determined as,

$$\varepsilon_{ij}(x_1, x_2) = \frac{1}{4\pi\sqrt{-1}}\sum_{\alpha=1}^{6}\frac{\eta_\alpha L_{s\alpha}b_s}{(x_1 + p_\alpha x_2)}\left(A_{i\alpha}\left(\delta_{1j} + p_\alpha\delta_{2j}\right) + A_{j\alpha}(\delta_{1i} + p_\alpha\delta_{2i})\right) \tag{13}$$

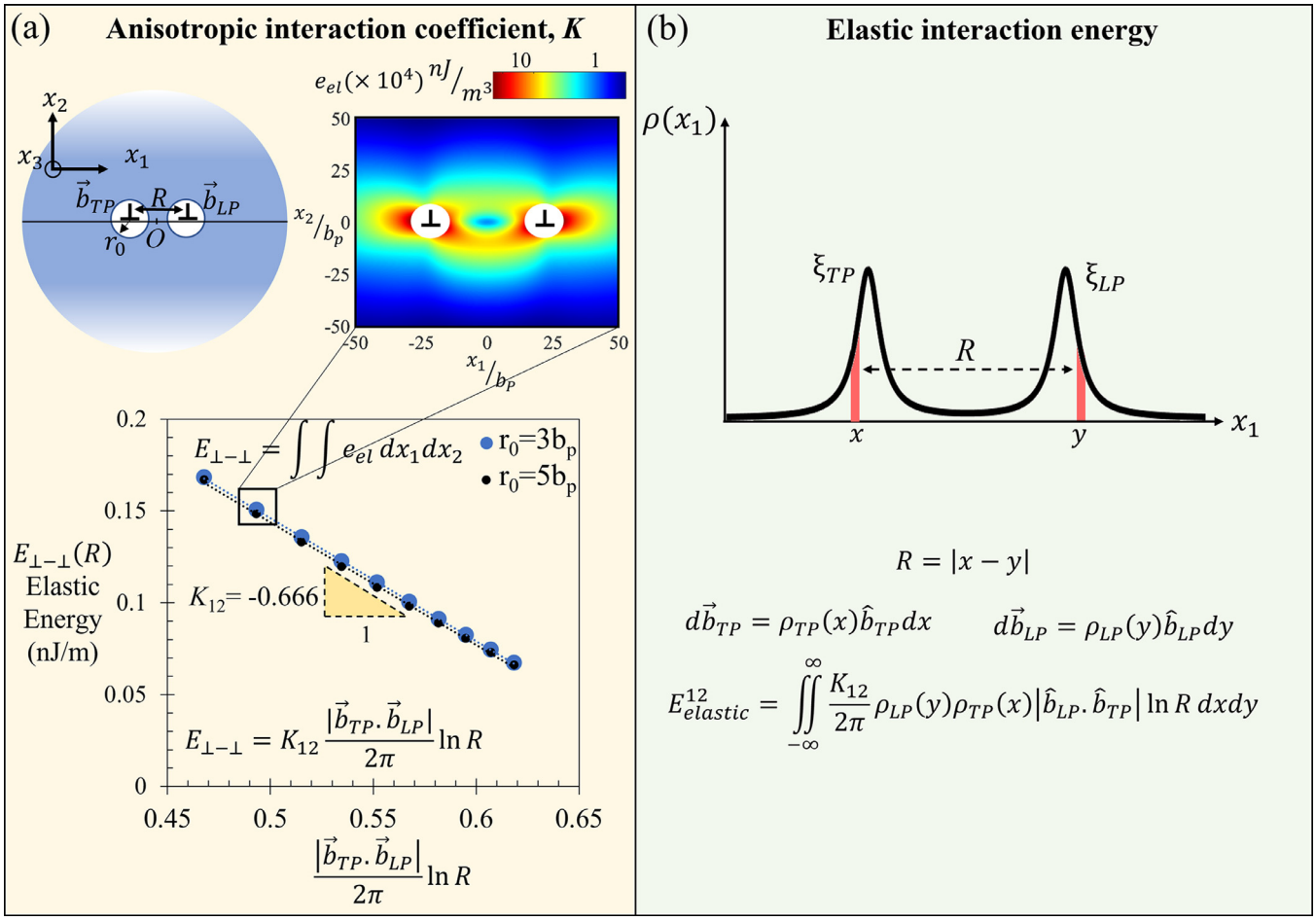

Fig. 3. Determining anisotropic interaction coefficient K to determine continuum strain-energy of $a/2\langle 011\rangle$ extended dislocation, illustrated using screw-character $a/2\langle 011\rangle$ dislocation in Ni (a) A system composed of the trailing partial, $\vec{b}_{TP}$, and leading partial, $\vec{b}_{LP}$, is considered, separated by distance R; the net strain-field around the partials is determined from the fully-anisotropy Eshelby-Stroh formalism, and the resulting contours of strain-energy density are shown ($b_P = |\vec{b}_{TP}| = |\vec{b}_{LP}|$); the strain-energy density is numerically integrated to yield the energy of interaction $E_{\perp-\perp}(R)$ as a function of the separation distance R, and the slope of variation of this function yields the anisotropic coefficient K_{12} (corresponding to the interaction between the trailing partial and leading partial); note that K_{12} is nearly identical for chosen core radius of $r_0 = 3b_P$; the coefficients of self-interaction K_{11} and K_{22} can be computed similarly (b) The strain-energy of interaction between the distributed cores of the trailing and leading partials is illustrated; the elastic interaction energy, $E^{12}_{elastic}$, is computed by integrating the interaction energy between infinitesimal fractionals $d\vec{b}_{TP}$ and $d\vec{b}_{LP}$, by utilizing the computed interaction coefficient K_{12} in (a); here $\hat{b}_{TP}$ and $\hat{b}_{LP}$ represent the unit vectors along the Burgers vectors of the trailing and leading partials respectively.

Table 1
Elastic constants (in GPa) of the FCC materials considered in this study.

Material	a_0(Å)	C_{11}	C_{12}	C_{44}	Ref.
Ni	3.52	261	151	132	[50]
Cu	3.61	171.2	123.8	75.6	[51]
Au	4.08	201	170	46	[50]
Ag	4.09	131.5	97.3	51.1	[50]
FeNiCoCrMn	3.6	221	152	165	[52]

In the current formulation, there are two partials with distinct Burgers vectors, $\vec{b}_{TP}$ and $\vec{b}_{LP}$, that are linearly independent of each other and hence require independent calculations of their E-S constants. The anisotropic E-S constants are determined for each of the partials, and the strain-fields corresponding to both partials, represented by $\varepsilon^{TP}_{ij}(x_1, x_2)$ and $\varepsilon^{LP}_{ij}(x_1, x_2)$ respectively, are determined from Eqs. (8) through (13). These strain-fields are then superposed to determine the net strain-field surrounding both dislocations. For this purpose, the relative position of both partials in space is necessary. It is assumed, without any loss in generality, that the trailing partial is at the position $(0, -R/2)$ and the leading partial is at position $(0, R/2)$. Subsequently, the total strain-field is given by the equation:

$$\varepsilon_{ij}(x_1, x_2, R) = \varepsilon^{TP}_{ij}\left(x_1 + R/2, x_2\right) + \varepsilon^{LP}_{ij}\left(x_1 - R/2, x_2\right) \tag{14}$$

The calculated strain-field ε_{ij} is then used to determine the spatially varying strain-energy density, given by:

$$e_{el}(x_1, x_2, R) = \frac{1}{2}C_{abcd}\varepsilon_{ab}(x_1, x_2, R)\varepsilon_{cd}(x_1, x_2, R) \tag{15}$$

where C_{abcd} are the components of the tensor of elastic constants in the $x_1 - x_2 - x_3$ system. The strain-energy density distribution is shown in Fig. 3 (a). Finally, the strain-energy per unit length of the dislocation line is calculated by spatially integrating the strain-energy density e_{el}, given by:

$$E_{\perp-\perp}(R) = \int_{-X_{max}}^{X_{max}}\int_{-X_{max}}^{X_{max}} e_{el}(x_1, x_2, R)\mathrm{d}x_1\mathrm{d}x_2 \tag{16}$$

The integral in Eq. (16) is done numerically, over a discretized grid employing a sufficiently fine grid size ($\Delta x_1/b_P = \Delta x_2/b_P \approx 0.2$) and large limit of integration ($X_{max} = 150b_P$) for convergence. The

Table 2
Anisotropic coefficients K_{11}, K_{12}, and K_{22} needed to compute the continuum strain-energy of the $^{a}/_{2}\langle 011\rangle$ extended dislocation (in units of $\times 10^2$ GPa).

Material	Edge-character of extended dislocation			Screw-character of extended dislocation		
	K_{11}	K_{22}	K_{12}	K_{11}	K_{22}	K_{12}
Ni	−1.1092	−1.1092	−1.3535	−0.9324	−0.9324	−0.6661
Cu	−0.5715	−0.5715	−0.7361	−0.4417	−0.4417	−0.2394
Au	−0.4282	−0.4282	−0.5774	−0.3204	−0.3204	−0.1525
Ag	−0.4346	−0.4346	−0.5612	−0.3409	−0.3409	−0.1969
FeNiCoCrMn	−1.0741	−1.0741	−1.3174	−0.8622	−0.8622	−0.5382

anisotropic interaction coefficient K_{12} that captures the strain-energy of interaction is given by the equation:

$$E_{\perp-\perp}(R) = C_0 + K_{12}\frac{\left|\vec{b}_{LP}\cdot\vec{b}_{TP}\right|}{2\pi}\ln R \tag{17}$$

where C_0 is a constant value independent of R. To determine the core-parameters $(\xi_{TP}, \xi_{LP}, s_1, s_2)$ of the $^{a}/_{2}\langle 011\rangle$ extended dislocation, it is only important to determine how the strain-energy of interaction changes with separation distance and thus C_0 is not relevant for this study. It is observed that the variation of $E_{\perp-\perp}(R)$ with $(\ln R)$ is predominantly linear, allowing the anisotropic coefficient K_{12} to be determined reliably from the slope of this variation, as shown in Fig. 3 (a). Following the same procedure elaborated above, the interaction coefficients K_{11} (or K_{22}) can be determined by considering the interaction between two dislocations with the same Burgers vectors $\vec{b}_{LP}$ (or $\vec{b}_{TP}$ respectively). The computed anisotropic interaction coefficients are listed in Table 2 below.

Once the interaction coefficients are known, the total continuum strain-energy $E_{STRAIN}(\xi_{TP}, \xi_{LP}, s_1, s_2)$ for the extended dislocation can be determined. This is done by integrating the strain-energy of interaction between infinitesimal fractional dislocations within each dislocation core. For instance, the energy of interaction between cores of the trailing and leading partial $E^{12}_{elastic}$ is illustrated in Fig. 3 (b). The total strain-energy additionally includes the self-interaction within the cores of the trailing and leading partials as well ($E^{11}_{elastic}$and $E^{22}_{elastic}$ respectively), given by the equation:

$$E_{STRAIN}(\xi_{TP}, \xi_{TP}, s_1, s_2) = E^{11}_{elastic} + E^{22}_{elastic} + E^{12}_{elastic} \tag{18}$$

where each summand is given by the equations:

$$\begin{aligned}
E^{11}_{elastic} &= \int_{-\infty}^{\infty}\int_{-\infty}^{\infty}\left({}^{K_{11}}/_{2\pi}\right)\rho_{TP}(x)\rho_{TP}(y)\ln|x-y|\mathrm{d}x\mathrm{d}y\\
E^{22}_{elastic} &= \int_{-\infty}^{\infty}\int_{-\infty}^{\infty}\left({}^{K_{22}}/_{2\pi}\right)\rho_{LP}(x)\rho_{LP}(y)\ln|x-y|\mathrm{d}x\mathrm{d}y\\
E^{12}_{elastic} &= \int_{-\infty}^{\infty}\int_{-\infty}^{\infty}\left({}^{K_{12}}/_{2\pi}\right)\rho_{TP}(x)\rho_{LP}(y)\left(\hat{b}_{TP}.\hat{b}_{LP}\right)\ln|x-y|\mathrm{d}x\mathrm{d}y
\end{aligned} \tag{19}$$

Each of the integrals in Eq. (19) is computed numerically, using the *integ* routine in MATLAB®, and subsequently added (as per Eq. (18)) to yield the continuum strain-energy of the extended dislocation $E_{STRAIN}(\xi_{TP}, \xi_{LP}, s_1, s_2)$.

2.2.2. Atomistic misfit energy: Wigner-Seitz cell misfit (WS-M) energy model

The misfit energy $E_{MISFIT}(\xi_{TP}, \xi_{LP}, s_1, s_2)$ captures the atomistic energies associated with disregistries $f_{TP,LP}(x_1)$ Eqs. (5) and ((6)) prevalent across the slip plane within the cores of both partials. These energies are determined from the Generalized Stacking Fault Energy (GSFE) curve of the slip system as mentioned in Section 1. The GSFE curve for a slip system is determined by calculating the atomistic potential energy $\gamma(\delta)$ corresponding to a planar disregistry δ introduced between two rigid halves of the crystal structure separated by the slip plane. This disregistry is introduced on the slip plane that separates the two halves along the direction of the Burgers vector of the slip system. The atomistic energies can be determined from atomistic simulation techniques such as Density Functional Theory (DFT) or Molecular Statics (MS). This brief description suffices for the purposes of our study and the reader is referred to [53] for a more detailed exposition on the GSFE curve.

Table 3
Fault Energies for fcc metals used in this study: intrinsic γ_{isf}; unstable γ_{us}.

Material	γ_{us} ($^{mJ}/_{m^2}$)	γ_{isf} ($^{mJ}/_{m^2}$)	Ref.
Ni	292	134	[54]
Cu	180	41	[55]
Au	134	33	[55]
Ag	133	18	[55]
FeNiCoCrMn	439	8	[52]

For the FCC system, two critical energy barriers decisively dictate the GSFE curve, namely the unstable stacking fauly energy barrier γ_{us} and the stable stacking fault energy barrier γ_{isf}. These barriers are listed in Table 3 for all materials considered in this study. The complete GSFE curve is given by the equation:

$$\gamma(\delta) = \begin{cases} \dfrac{\gamma_{us}}{2}\left(1-\cos\left(\dfrac{2\pi\delta}{b_P}\right)\right) \text{for } 0 \le \delta \le \dfrac{b_P}{2} \text{ or } \dfrac{3b_P}{2} \le \delta \le 2b_P \\ \gamma_{isf} + \left(\dfrac{\gamma_{us}-\gamma_{isf}}{2}\right)\left(1-\cos\left(\dfrac{2\pi\delta}{b_P}\right)\right) \text{for } \dfrac{b_P}{2} \le \delta \le \dfrac{3b_P}{2} \end{cases} \tag{20}$$

However, it must be noted that there are two Shockley partials with distinct Burgers vectors in this system, and the fault energy curve corresponding to each partial must be partitioned, as done here. The GSFE curve corresponding to both the trailing and leading partials are given by the equations:

$$\gamma_{TP}(\delta) = \begin{cases} \dfrac{\gamma_{us}}{2}\left(1-\cos\left(\dfrac{2\pi\delta}{b_P}\right)\right) \text{for } 0 \le \delta \le \dfrac{b_P}{2} \\ \gamma_{isf} + \left(\dfrac{\gamma_{us}-\gamma_{isf}}{2}\right)\left(1-\cos\left(\dfrac{2\pi\delta}{b_P}\right)\right) \text{for } \dfrac{b_P}{2} \le \delta \le b_P \end{cases} \tag{21}$$

$$\gamma_{LP}(\delta) = \begin{cases} \gamma_{isf} + \left(\dfrac{\gamma_{us}-\gamma_{isf}}{2}\right)\left(1-\cos\left(\dfrac{2\pi\delta}{b_P}\right)\right) \text{for } 0 \le \delta \le \dfrac{b_P}{2} \\ \dfrac{\gamma_{us}}{2}\left(1-\cos\left(\dfrac{2\pi\delta}{b_P}\right)\right) \text{for } \dfrac{b_P}{2} \le \delta \le b_P \end{cases} \tag{22}$$

Having described the GSFE curve for the slip system, the subsequent and, perhaps, the most critical step is to interpret the energy-barriers into the misfit-energy for the extended dislocation, for a given length L of the dislocation line. This step involves the disregistry function and a spatial summation over discrete lattice positions on the slip plane. Conventionally, the following Simple-Cubic-Row-Misfit (SC-M) model for the misfit-energy has been used in literature:

$$E^{SC-M}_{MISFIT} = \sum_{m=-\infty}^{\infty}\gamma\left(f\left(ma'\right)\right)\left(a'L\right) \tag{23}$$

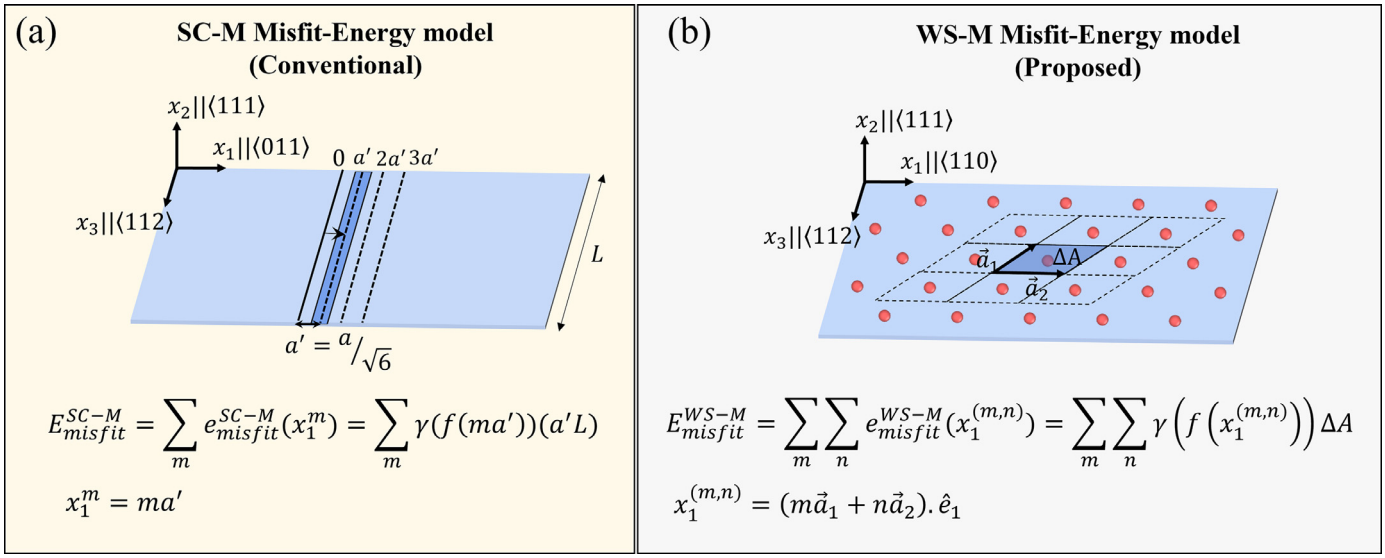

Fig. 4. Analytical models for misfit energy: (a) Conventional Simple-Cubic-Row-Misfit (SC-M) energy calculation where the underlying lattice is modeled as rows of atoms parallel to the dislocation line direction x_3, spaced along x_1 at a discrete periodic distance a'; the magnitude of a' is postulated to be the interplanar spacing along x_1, which for the given crystallographic directions is $a' = a/\sqrt{6}$; the misfit energy is taken as the sum of fault-energies $e^{SC-M}_{misfit}(x_1^m)$ at each discrete position $x_1^m = ma'$ over the shaded region with area $(a'L)$ (b) Proposed Wigner-Seitz Cell Misfit (WS-M) misfit energy calculation in this study, where the atomic structure of the underlying slip-plane lattice is captured; lattice vectors $\vec{a}_1$ and $\vec{a}_2$ are defined to map out all atomic sites on the slip plane, and the area ΔA is the Wigner-Seitz (W-S) cell area around each atomic site; the misfit energy is a two-dimensional sum of fault-energies $e^{WS-M}_{misfit}(x_1^{(m,n)})$ at each atomic site $x_1^{(m,n)} = (m\vec{a}_1 + n\vec{a}_2).\hat{e}_1$ taken over the shaded W-S area; the spacing between consecutive atomic-rows, for the given crystallographic orientation, is given by $0.5|\vec{a}_1| = 1.5a/\sqrt{6}$ which is not equal to the magnitude of a' defined previously in the conventional SC-M model (refer main text for crystallographic definition of $\vec{a}_1$).

where the underlying lattice on the slip plane is modeled as rows of atoms parallel to the dislocation line (i.e. parallel to x_3) spaced apart by magnitude a' perpendicular to the dislocation line (i.e. along x_1; refer Fig. 2(a) for the coordinate system), γ is given by Eq. (20) and f by Eq. (3). In short, the SC-M model determines the magnitude of disregistry $u = f(x_1^m)$, at each discrete position $x_1^m = ma'$, and adds the energy cost associated with the disregistries i.e. summation of $\gamma(f(x_1^m = ma'))$, weighted with a planar area $(a'L)$ parallel to the dislocation line. This SC-M model of the underlying lattice dates back to the original work of Peierls [9], over 80 years back, where an expression for the lattice restoring force was first proposed and a simple-cubic lattice structure was chosen as the ansatz. It has since been widely adopted in several works such as those in refs. [13,17,24,38,46,56,57]. The finite magnitude of a' represents the discreteness of the underlying lattice and this value cannot be chosen arbitrarily. Till date, the value chosen for a' is the magnitude of the interplanar spacing along x_1 i.e. perpendicular to the dislocation line and on the slip-plane. The SC-M misfit energy model is schematically represented in Fig. 4(a).

There are multiple challenges with the conventional SC-M misfit-energy model which the current study proposes to improve upon. The primary drawback of the conventional SC-M model is that it does not account for the lattice structure of the slip-plane, where the positioning of individual atomic sites depends on multiple factors such as the parent crystal structure, crystallography of the slip-plane and the character of the dislocation. Secondly, the spacing between consecutive rows of atomic sites on the slip plane is not equal to the interplanar spacing which is the value chosen for a' (indicated in Fig. 4(b)). Furthermore, the cell-area ascribed to each atomic-site depends on both of the aforementioned factors and requires more fundamental grounding than the rectangular area assigned to each atomic-row (i.e. $(a'L)$ in Fig. 4(a) and in Eq. (23)) in the SC-M model. This study proposes a novel Wigner-Seitz Cell Misfit (WS-M) model which improves on all of the above aspects and further advances the concept of discrete a'-spacing to the discrete Wigner-Seitz (W-S) cell area surrounding each atomic site on the slip plane. This is schematically represented in Fig. 4(b).

The WS-M model defines two lattice-vectors on the slip plane, given by $\vec{a}_1$ and $\vec{a}_2$ such that every lattice site on the slip plane is given by $\vec{x}^{(m,n)} = m\vec{a}_1 + n\vec{a}_2$, for integers $m, n \in \mathbb{Z}$. These vectors are crystallographic lattice vectors that depend on the parent crystal structure (FCC, in this case) and the crystallography of the slip plane ({111} slip plane in this case). These vectors define a primitive-cell for the slip-plane lattice, given by the shaded region in Fig. 4(b). The reader is referred to ref. [58] for a detailed coverage of concepts of primitive cell and the Wigner-Seitz (W-S) cell. The area enclosed within the cell is the same as the area of the W-S cell of the slip-plane lattice, illustrated schematically in Fig. 5, and is a property unique to the slip-plane lattice. With the proposed advancements, the expression for the misfit energy is given by the equation:

$$E^{\text{WS-M}}_{MISFIT} = \sum_{m=-\infty}^{\infty} \sum_{n=-\infty}^{\infty} \gamma\left(f\left((m\vec{a}_1 + n\vec{a}_2).\hat{e}_1\right)\right)(\Delta\text{A}) \tag{24}$$

where ΔA is the area of the W-S cell around each atomic site at position $\vec{x}_1^{(m,n)} = m\vec{a}_1 + n\vec{a}_2$, γ is given by Eq. (20) and f by Eq. (3). Note that the vectors $\vec{a}_1$ and $\vec{a}_2$ are two-dimensional, defined on the slip-plane of the dislocation which is the plane defined by the $x_1 - x_3$ axes. The disregistry function f is however only a function x_1, therefore the argument for the disregistry function in Eq. (24) is the x_1 component at each atomic-site given by $(m\vec{a}_1 + n\vec{a}_2).\hat{e}_1$, alternatively represented as $x_1^{(m,n)}$ in Fig. 4 (b). Also note that depending on the character of the extended dislocation, the orientation of the lattice with respect to the global $x_1 - x_2 - x_3$ axes changes (as seen in the distinct coordinate systems defined in Section 2.1 previously). Consequently, the individual atomic positions around the dislocation changes with character. The distinct lattice orientations and,consequently, atomic positions are illustrated in Fig. 6 for edge and screw natures of the extended dislocation. These features are successfully captured by the proposed WS-M framework by defining the lattice vectors, $\vec{a}_1$ and $\vec{a}_2$, appropriately for each case at distinct orientations relative to the global axes on the $x_1 - x_3$ slip-plane (i.e. the $(1\bar{1}1)$ plane). Note that in either case, the a' definition employed by the conven-

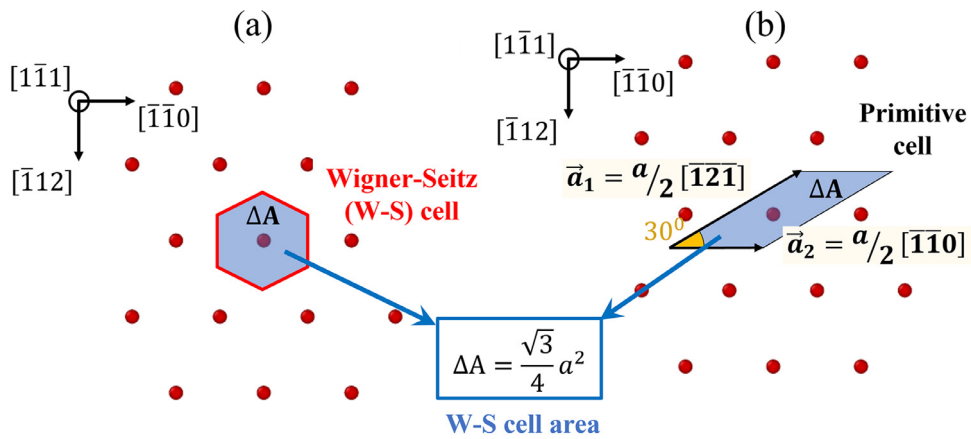

Fig. 5. Schematic illustration of (a) the Wigner-Seitz (W-S) cell of the {111} slip-plane lattice and (b) the primitive-cell used for the proposed WS-M misfit-energy model; the area enclosed by both cells, ΔA, is the same i.e. the W-S cell area, and is a property unique to the lattice, depending on the lattice-constant a as shown.

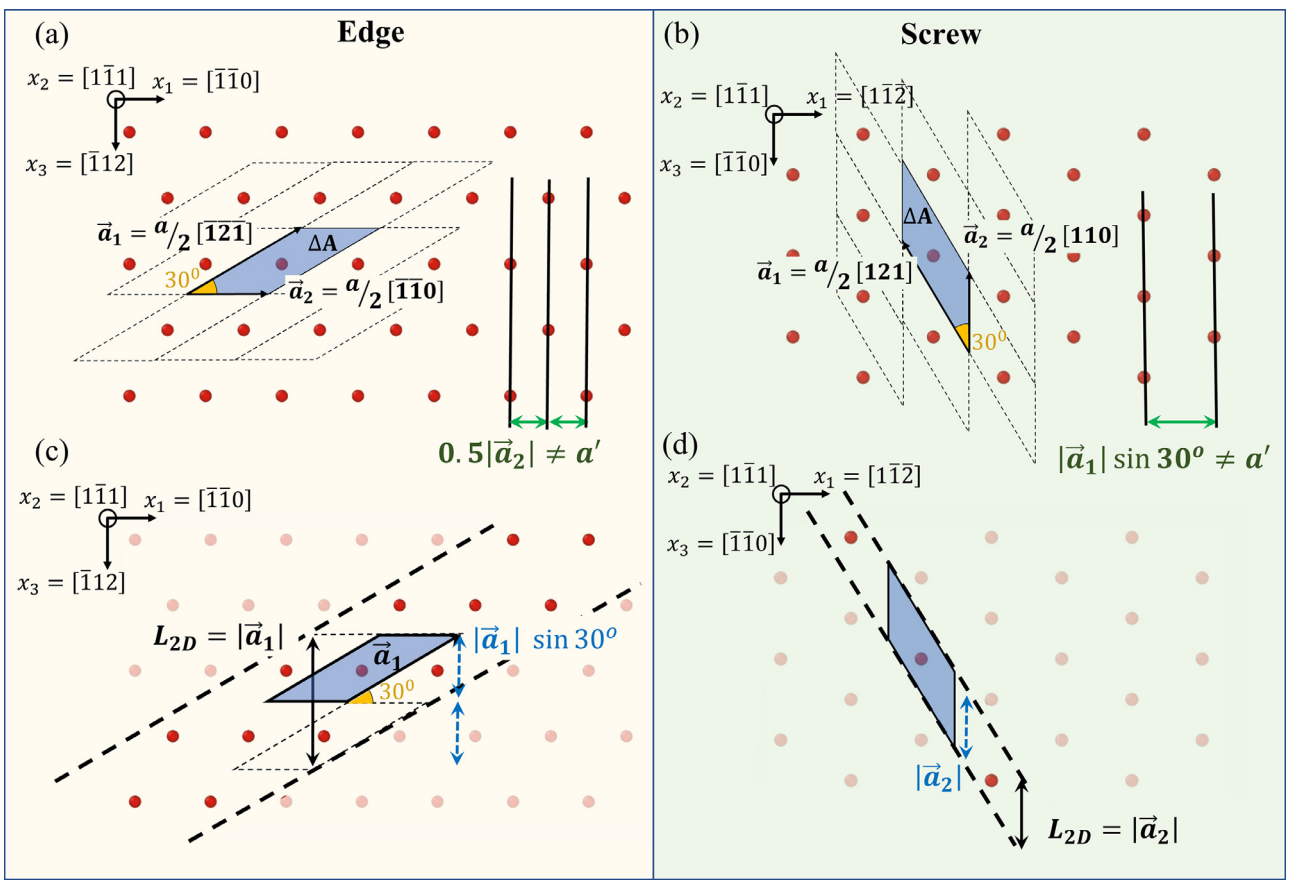

Fig. 6. Lattice structure of the {111} slip plane, for edge and screw character of the $a/2\langle 011\rangle$ extended dislocation considered in this study: (a) Individual atomic positions on the slip-plane are shown, along with the lattice vectors $\vec{a}_1$, $\vec{a}_2$ and the W-S area; the relative orientation of the lattice vectors with respect to the dislocation line direction (parallel to x_3) is dictated by the character of the dislocation (edge character in this case); the shaded cell is the primitive cell for the lattice-structure on the slip-plane adopted by the proposed WS-M approach; the actual atomic-spacing on the slip-plane does not match the a' value adopted by the conventional SC-M approach, which is the interplanar spacing along x_1 ([$\bar{1}\bar{1}$0] in this case) (b) Individual atomic positions on the slip-plane are shown, along with the lattice vectors $\vec{a}_1$, $\vec{a}_2$ and the W-S area; the relative orientation of the lattice vectors with respect to the dislocation line direction (parallel to x_3) is dictated by the character of the dislocation (screw character in this case); the shaded cell is the primitive cell for the lattice-structure on the slip-plane adopted by the proposed WS-M approach; the actual atomic-spacing on the slip-plane does not match the a' value adopted by the SC-M approach, which is the interplanar spacing along x_1 ([$1\bar{1}\bar{2}$] in this case) (c) The edge-case slip-plane lattice structure can be reproduced by periodic repetition of the emphasized atomic-sites within a band of length $L_{2D} = |\vec{a}_1|$ along the dislocation line; such a reduction is useful to feasibly compute the summation for the misfit energy (d) The screw-case slip-plane lattice structure can be reproduced by periodic repetition of the emphasized atomic-sites within a band of length $L_{2D} = |\vec{a}_2|$ along the dislocation line; such a reduction is useful to feasibly compute the summation for the misfit energy.

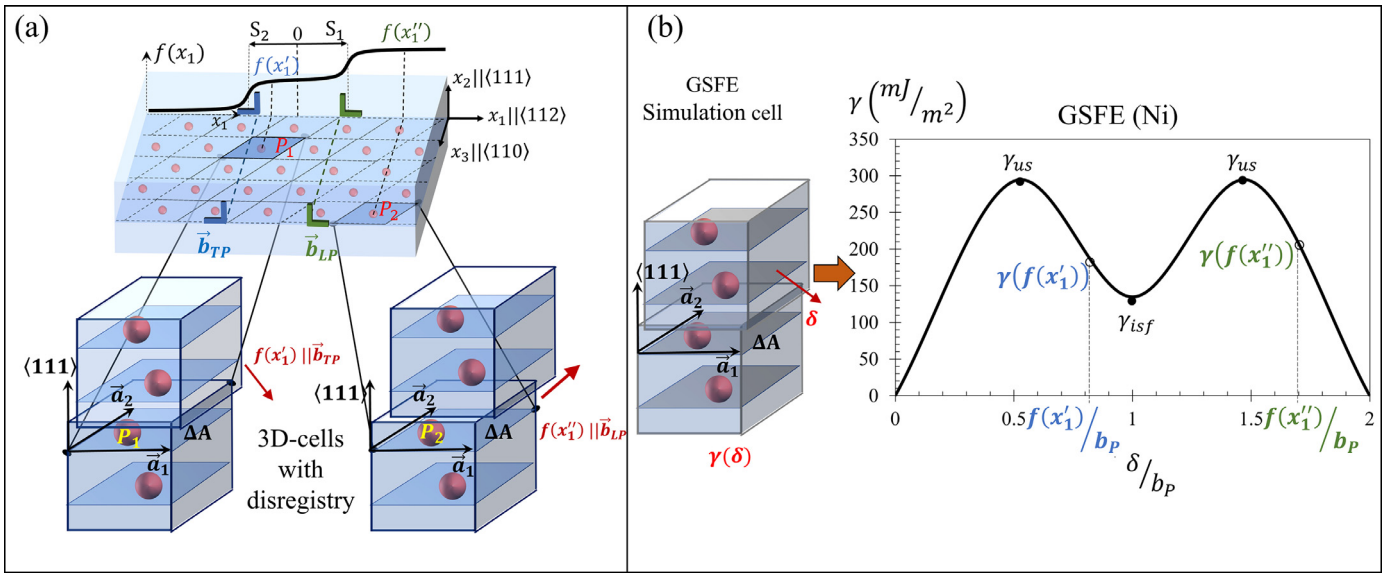

Fig. 7. Direct correspondence between the misfit-energy of the system and the fault-energy barriers on the GSFE curve: (a) Atomic-structure of the slip-plane showing the positions of the trailing and leading partials with Burgers vectors $\vec{b}_{TP}$ and $\vec{b}_{LP}$ respectively; the disregistry distribution $f(x_1)$ is also plotted; consider the atomic-sites P_1 and P_2 where the magnitude of disregistry is given by $f(x'_1)$ and $f(x''_1)$ respectively; the stack of atoms on {111} planes above and below each respective site P_1 and P_2 are shown, within the Wigner-Seitz (W-S) area ΔA bounded by the lattice-vectors $\vec{a}_1$ and $\vec{a}_2$; these atoms constitute a 3D-cell housing a planar disregistry and the misfit-energy cost corresponding to the disregistry is given by the (b) A schematic representation of the simulation cell used to determine the Generalized Stacking Fault Energy (GSFE) curve, involving the lattice-vectors W-S area and planar disregistry identical to the 3D-cells in (a); the atomistic potential energy $\gamma(\delta)$ corresponding to planar disregistry δ is computed; the GSFE curve, plotted for Ni here, is shown from which the misfit-energies $\gamma(f(x'_1))$ and $\gamma(f(x''_1))$, at sites P_1 and P_2 respectively, can be determined.

tional SC-M approach does not match the actual atomic-spacing on the slip-plane lattice.

The WS-M two-dimensional summation covering each atomic-site can be further reduced based on the symmetry of the slip-plane lattice. For instance, as shown in Figs. 6 (c, d), the atomic positions on the slip-plane for edge and screw character of the $a/2\langle 011\rangle$ extended dislocation can be described by periodic images of a narrow band of atomic-sites, repeating periodically along the dislocation line over a spacing of L_{2D}. Consequently, the misfit-energy expression in Eq. (24) can be expressed as:

$$E_{MISFIT}(\xi_{TP}, \xi_{LP}, s_1, s_2) = \frac{1}{L_{2D}} \sum_{m=-\infty}^{\infty} \sum_{n=-N_0}^{N_0} \gamma\left(f\left((m\vec{a}_1 + n\vec{a}_2).\hat{e}_1\right)\right)(\Delta A) \tag{25}$$

where $(L_{2D}, N_0) = (|\vec{a}_1|, 1)$ for the case of a $a/2\langle 011\rangle$ edge-dislocation, and $(L_{2D}, N_0) = (|\vec{a}_2|, 0)$ for the screw-dislocation case, γ is given by Eq. (20) and f by Eq. (3). The energy is normalized by the length L_{2D} to yield a misfit-energy measure that is normalized per unit length of the dislocation line.

The description of the misfit-energy using lattice-vectors and W-S cell area has further significance. The lattice-vectors bounding the W-S area represent the smallest periodic primitive cell on the slip-plane, as shown in Fig. 6 (a, b). It is precisely the same cell that is employed in the calculation of the fault-energy curve $\gamma(\delta)$ using methods such as DFT, alluded to at the beginning of this subsection. For instance, consider the slip-plane lattice in Fig. 7 (a). On this plane, there is a disregistry distribution $f(x_1)$ introduced by the combination of the two Shockley partials, $\vec{b}_{TP}$ and $\vec{b}_{LP}$, constituting the $a/2\langle 011\rangle$ extended dislocation considered in this study. Now consider an arbitrary atomic-site on this slip-plane, say P_1, shown in Fig. 7 (a). Consider the stack of atoms on the {111} planes above and below P_1, within the W-S area defined around the site, also shown in Fig. 7 (a). This stack of atoms and the W-S area define a three-dimensional (3D) cell which would have been in perfect FCC arrangement if not for the disregistry $f(x'_1)$ on the slip-plane at P_1. The set of all 3D cells constructed around each atomic-site on the slip-plane yields the complete 3D crystal structure around the extended dislocation. If the "per-site" misfit-energy corresponding to the disregistry within each 3D cell is known, then the aggregate sum of such misfit-energies over each atomic-site yields the total misfit-energy of the system. It is elegant to note that the per-site misfit-energy is known directly from the GSFE curve because the curve itself is obtained by simulations of disregistry introduced in a "simulation cell" identical to the 3D-cell defined at each site (refer Fig. 7 (b)). Thus, there is a direct geometric correspondence that has been established between the method of simulation to obtain the GSFE curve and its consequent application on the plane of disregistry of a dislocation to obtain the misfit-energy. Consequently, at site P_1, for a disregistry of $\delta = f(x'_1)$ introduced along $\vec{b}_{TP}$, the misfit-energy is equal to $\gamma(f(x'_1))$ obtained directly from the GSFE curve as shown in Fig. 7 (b). Furthermore, since the GSFE curve is generally computed by allowing atomic-relaxations normal to the slip plane, directly sampling the same fault-energy allows the WS-M model to inherit incorporation of such normal relaxations at each atomic-site. However, the magnitudes of these relaxations cannot be predicted but only their influence is captured through use of fault-energies from the GSFE curve. By maintaining such a close correspondence between the energies computed on the GSFE curve and the misfit-energies within the crystal structure around the dislocation, it is asserted that the proposed framework leads to an accurate determination of the misfit-energy, advancing over prior frameworks. Nonetheless, it must be mentioned that one of the effects that cannot yet be captured in the current framework is the coupled-influence of a varying disregistry distribution on the fault-energy at each atomic-site. This would be a promising avenue for future research to further improve the predictive accuracy of the proposed framework.

A direct comparison between the conventional SC-M approach and the WS-M approach of the present study is shown in Fig. 8. The distribution of $e^{SC-M}_{misfit}(x_1^m) = \gamma(f(x_1^m))a'$ and $e^{WS-M}_{misfit}(x_1^{(m,n)}) =$

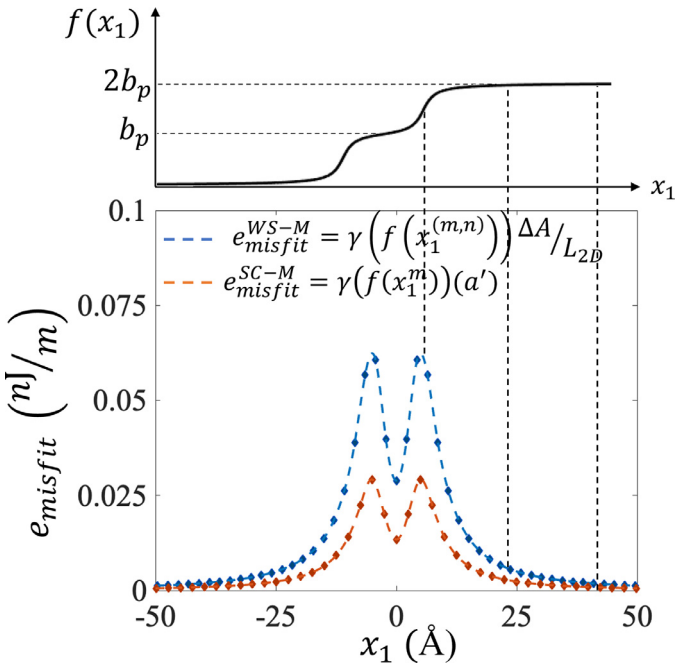

Fig. 8. Comparison of the conventional SC-M and proposed WS-M approach for misfit-energy determination, noting a significant difference between predictions of the two approaches (the misfit-energies are computed for the case of the $a/2\langle 011\rangle$ extended dislocation of screw-character in material Ni).

$\gamma(f(x_1^{(m,n)}))\Delta A/L_{2D}$ are respectively shown, both of which represent the local misfit energy at distinct lattice sites, $x_1^m = ma'$ and $x_1^{(m,n)} = (m\vec{a}_1 + n\vec{a}_2).\hat{e}_1$, for the SC-M and WS-M approaches respectively. The proposed WS-M approach yields improved predictions for the misfit-energy as compared to the SC-M approach, validated by the agreement of the predicted CRSS with existing experimental measurements in literature, shown later in this study, in Section 3.

The expression for the misfit-energy is rewritten in terms of the partitioned fault-energies (given by Eqs. (21) and (22)) and disregistry functions of the individual Shockley partials (given by Eqs. (5) and (6)), the total misfit energy of the system is given by the equation:

$$E_{MISFIT}(\xi_{TP}, \xi_{LP}, s_1, s_2) = \frac{1}{L_{2D}}\left[\begin{array}{l}\sum_{n=-N_0}^{N_0}\sum_{m=-M_{\max}}^{-1}\gamma_{TP}\left(f_{TP}\left(x_1^{(m,n)}\right)\right)\Delta A \\ \ldots\ldots + \sum_{n=-N_0}^{N_0}\sum_{m=0}^{M_{\max}}\gamma_{LP}\left(f_{LP}\left(x_1^{(m,n)}\right)\right)\Delta A\end{array}\right] \tag{26}$$

where $x_1^{(m,n)} = (m\vec{a}_1 + n\vec{a}_2).\hat{e}_1$. A large summation limit of $M_{\max}$ is chosen, of the order of 10^4, at which the computed misfit energy $E_{MISFIT}(\xi_{TP}, \xi_{LP}, s_1, s_2)$ is sufficiently converged. The misfit-energy given by Eq. (26) is calculated per unit length of the dislocation-line. Now, the misfit energy can be computed as a function of the core parameters $(\xi_{TP}, \xi_{LP}, s_1, s_2)$ of the extended dislocation.

2.2.3. Determination of core-structure parameters

At this stage, the continuum elastic energy $E_{ELASTIC}(\xi_{TP}, \xi_{LP}, s_1, s_2)$ and the atomistic misfit energy $E_{MISFIT}(\xi_{TP}, \xi_{LP}, s_1, s_2)$ are known as a function of the dislocation core-parameters $(\xi_{TP}, \xi_{LP}, s_1, s_2)$ from Eqs. (18) and (26) respectively. Thus, the total energy of the $a/2\langle 011\rangle$ extended dislocation $E_{TOT}(\xi_{TP}, \xi_{LP}, s_1, s_2)$ is also known as a function of the core-parameters from Eq. (7). The core-parameters minimizing E_{TOT} are sought by solving the equations

$$\frac{\partial E_{TOT}}{\partial \xi_{TP}} = 0;\ \frac{\partial E_{TOT}}{\partial \xi_{LP}} = 0;\ \frac{\partial E_{TOT}}{\partial s_1} = 0;\ \frac{\partial E_{TOT}}{\partial s_2} = 0 \tag{27}$$

The minimization routine is implemented using the *fmincon* routine in MATLAB®. The minimizing parameters $(\xi_{TP}^0, \xi_{LP}^0, s_1^0, s_2^0)$ are then used to determine the CRSS. The variation of the total energy about the energy-minimizing solution $(\xi_{TP}^0, \xi_{LP}^0, s_1^0, s_2^0)$ is plotted in Figs. 9 and 10, illustrated for the case of a screw-character $a/2\langle 011\rangle$ extended dislocation in Ag. Fig. 9 plots the variation of total energy against varying combinations of (s_1, s_2) which represent the positions of the leading and trailing Shockley partials respectively. The core-widths for the partials are fixed at (ξ_{TP}^0, ξ_{LP}^0). Note that the elastic and misfit energy display monotonic trends of opposing nature, as shown in Fig. 9 (a, b). The elastic-energy increases with reducing $d = s_1 + s_2$, which is the fault-width between the partials. This is because the separation distance between the dislocation cores is reducing and raises the elastic-energy of interaction. Contrastingly, the misfit-energy increases with increasing $d = s_1 + s_2$ because the faulted-region of the dislocation cores is now spread over a larger distance, thereby raising its total misfit-energy. Thus there exists a position (s_1^0, s_2^0) at which a balance between the two energies is achieved to minimize the total energy E_{TOT}

The misfit energy has further undulations on a smaller magnitude scale revealed by doing a line-scan of the misfit-energy landscape across points $A_M O_M B_M$ (subscript M representing misfit), as shown in Fig. 9 (b) and plotted in 9 (c). There is a condition that is satisfied along this line which is that $s_1 + s_2 = C$, a constant, implying that the stacking-fault width between the partials remains the same. The undulating misfit-energy curve in Fig. 9 (c) reveals the existence of multiple local minima $O_M^i = (s_1^i, s_2^i)$ where the extended dislocation has the same misfit-energy. This corresponds exactly to the existence of multiple energetically-degenerate positions for the Shockley partials on the slip-plane lattice. The existence of such energetically-degenerate positions is further illustrated in the landscape of E_{TOT} in Fig. 9 (d), where analogous minima in total-energy exist at positions $O = (s_1^0, s_2^0)$, $O_1 = (s'_1, s'_2)$ etc. Thus these minima represent multiple energetically-stable positions of the $a/2\langle 011\rangle$ extended dislocation on the {111} slip-plane.

The variation of the total energy E_{TOT} with the core-widths of the partials (ξ_{TP}, ξ_{LP}) is shown in Fig. 10, plotted at positions (s_1^0, s_2^0). Again, the elastic and misfit energy display monotonic trends of opposing nature, as shown in Fig. 10 (a, b). The elastic-energy increases with reducing core-widths. This is because the separation distances between fractional-dislocations within the dislocation cores are reducing, raising their elastic-energy of interaction. Contrastingly, the misfit-energy increases with increasing core-widths because the dislocation cores are spread over a larger span, increasing the total area of misfit and ultimately raising the misfit-energy. The total energy is minimized at core-widths (ξ_{TP}^0, ξ_{LP}^0) where a balance between the two opposing trends is achieved. Thus the equilibrium core-configuration of the $a/2\langle 011\rangle$ extended dislocation is described by the core-parameters $(\xi_{TP}^0, \xi_{LP}^0, s_1^0, s_2^0)$ and the equilibrium configurations are plotted in Fig. 11 for extended dislocations of edge and screw characters. Recall that in each case, the individual Shockley partials are of a mixed character and the framework developed in the present study is capable of predicting their core-structure. The core-widths of the individual partials and the fault-width separating them differ considerably between the edge and screw characters. The methodology for prediction of the CRSS is presented in the next subsection.

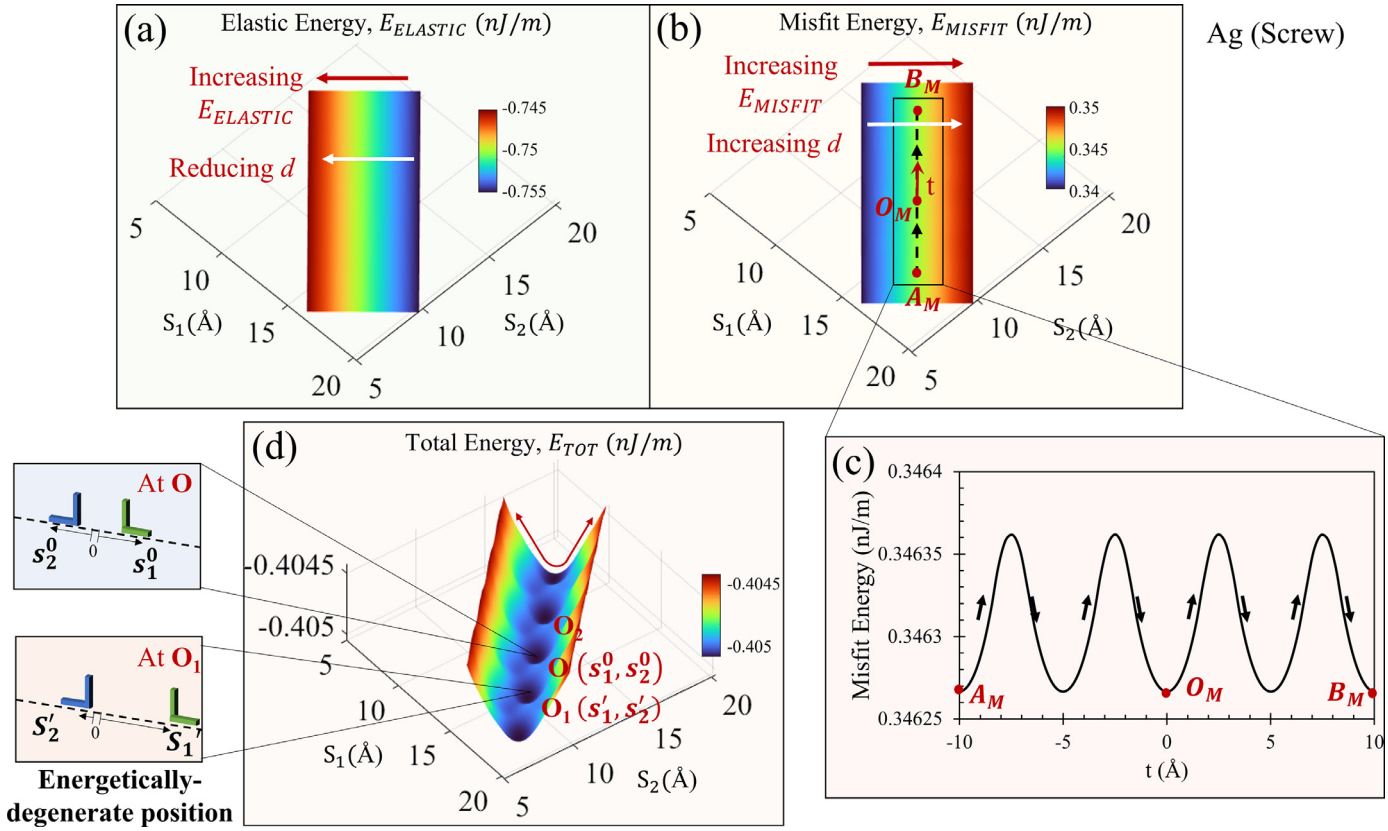

Fig. 9. Variation of elastic $E_{ELASTIC}$, misfit E_{MISFIT}, and total energies E_{TOT} of the $^a/_2\langle 011\rangle$ extended dislocation plotted against the positions of leading and trailing partials (s_1, s_2) respectively at the energy-minimizing core-widths (ξ_{TP}^0, ξ_{LP}^0) (shown here for the case of screw-character dislocation Ag); Variation of (a) elastic energy $E_{ELASTIC}$ and (b) misfit energy E_{MISFIT}, displaying opposing monotonic trends with respect to change in stacking-fault width $s_1 + s_2 = d$ (c) Plot of the misfit-energy over a selected path $A_M O_M B_M$ shown in (b) illustrating the existence of multiple energy minima on the landscape (d) Plot of the total energy E_{TOT} also illustrating the existence of multiple minima $O(s_1^0, s_2^0)$, $O_1(s'_1, s'_2)$ etc., each of which represents an energetically-degenerate position for the extended dislocation (as shown in the schematic insets); these minima lie along the line $s_1 + s_2 = C$, a constant, implying that in each of these positions the stacking-fault width between the partials is the same.

2.3. CRSS of $^a/_2\langle 011\rangle$ extended dislocation

The proposed framework is motivated from the Peierls-Nabarro (P-N) model [10] and advances the model to determine the CRSS of $^a/_2\langle 011\rangle$ extended dislocation in FCC materials. In short, the CRSS is determined from the maximum gradient on the energy landscape. In the standard P-N approach, only the 1D misfit-energy landscape is considered. In this study, a novel approach is proposed where the total-energy landscape, E_{TOT} is considered. The variation of the total-energy against the position of the individual Shockley partials is of interest i.e. Fig. 9 (c). The total-energy landscape is plotted again in Fig. 12(a) below, shown for a screw-character $^a/_2\langle 011\rangle$ dislocation in Ni. As discussed in Section 2.2.3 before, the total-energy landscape has multiple energetically-degenerate minima represented by points $O = (s_1^0, s_2^0)$, $O_1 = (s'_1, s'_2)$, etc., each representing an energetically stable position of the extended dislocation on the slip-plane.

To determine the CRSS, the energy-trajectory undergone by the $^a/_2\langle 011\rangle$ extended dislocation in moving from one minimum, say O, to the next energetically-degenerate position, say O_1, must be extracted. The energy trajectory depends on how the individual positions of the Shockley partials (s_1, s_2) vary in moving from O to O_1. This variation in positions between the minima effectively represents the "path" taken by the $^a/_2\langle 011\rangle$ extended dislocation. In the proposed approach, the "Minimum-Energy Path" (MEP) between the two minima is determined, along which the dislocation faces the least resistance to motion. For this purpose, a set of paths between the two minima is considered, given by $(s_1(t), s_2(t))$, with the path being parametrized by a monotonically increasing variable t. Considering the path to begin at the minimum O, it is known that for $t = 0$, $s_1^0 = s_1(0)$ and $s_2^0 = s_2(0)$. Also, every allowable path must exhibit a periodicity along the straight line $s_1 + s_2 = C$ (passing through O and O_1, shown by the dashed line in Fig. 12 (a)), which is to say that at periodic intervals along the path, the stacking-fault width between the partials recovers to its equilibrium value $C = s_1^0 + s_2^0$ that it began with at O. The trajectory that connects the minima must be periodic function, connecting all the energetically-degenerate states lying at periodic intervals on the total-energy landscape. Therefore, a Fourier-series based model is chosen to define the path, described by the equations:

$$\begin{aligned} s_1(t) &= s_1^0 + \left(\tfrac{1}{\sqrt{2}}\right)\left(t + C_0 + \sum_{k=1}^{n} C_k\left(1 - \cos\tfrac{2k\pi t}{C_P}\right)\right) \\ s_2(t) &= s_2^0 + \left(\tfrac{1}{\sqrt{2}}\right)\left(-t + C_0 + \sum_{k=1}^{n} C_k\left(1 - \cos\tfrac{2k\pi t}{C_P}\right)\right) \end{aligned} \tag{28}$$

where the maximum number of periodic functions chosen is taken to be $n = 4$, sufficient for the purposes of the study. Thus, the set of parameters $(C_0, C_1, C_2, C_3, C_4, C_P)$ define a path on the total-energy landscape beginning at O. Note that the straight-path connecting O and O_1 is modeled by the parameter values $C_0 = C_1 = C_2 = C_3 = C_4 = 0$, and for any $C_P \neq 0$. For a different set of parameter values, the path is not straight but zig-zag in nature (shown by the solid-line path in Fig. 12 (a)). The energy is computed at discretized points along the path, given by $t_i = i\Delta t$, where $\Delta t = 0.01$ Å. The total cumulative energy along the path is summed to obtain the

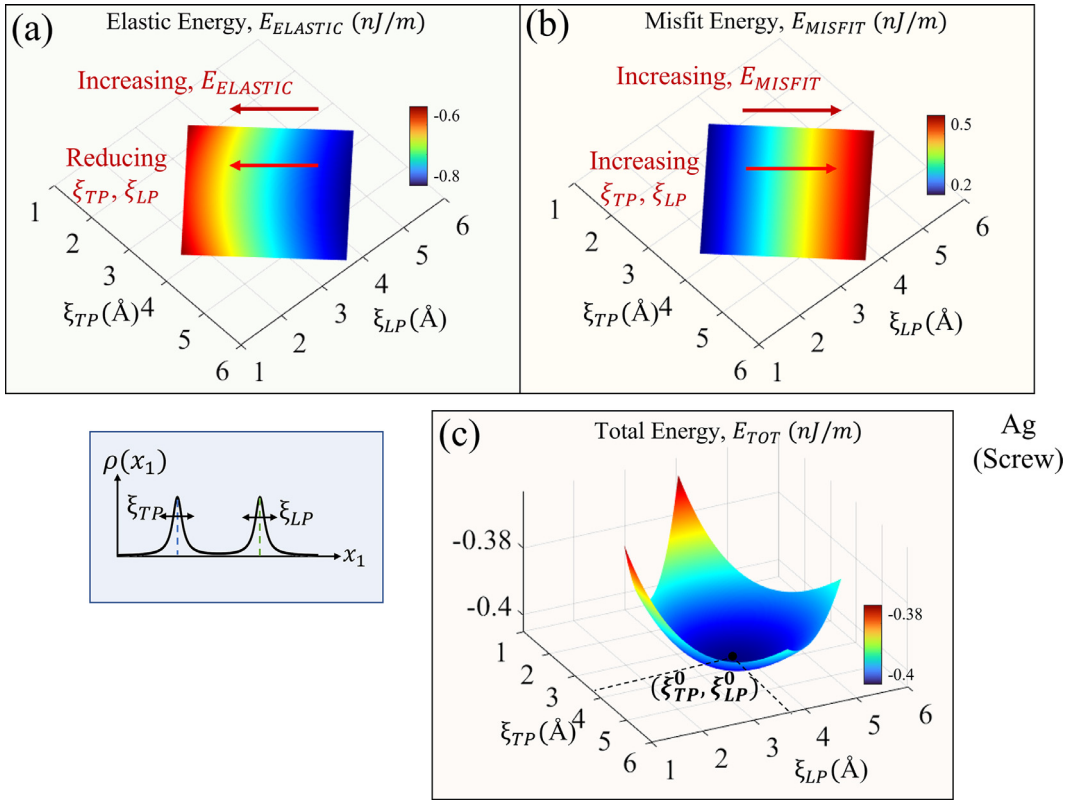

Fig. 10. Variation of elastic $E_{ELASTIC}$, misfit E_{MISFIT}, and total energies E_{TOT} of the $a/2\langle 011\rangle$ extended dislocation plotted against the core-widths of trailing and leading partials (ξ_{TP}, ξ_{LP}) respectively at the energy-minimizing positions of the partials (s^0_1, s^0_2) (shown here for the case of screw-character dislocation Ag); Variation of (a) elastic energy $E_{ELASTIC}$ and (b) misfit energy E_{MISFIT}, displaying opposing monotonic trends with respect to the partial core-widths (ξ_{TP}, ξ_{LP}), summing together to yield (c) the total-energy E_{TOT} behavior which exhibits a minimum at (ξ^0_{TP}, ξ^0_{LP}).

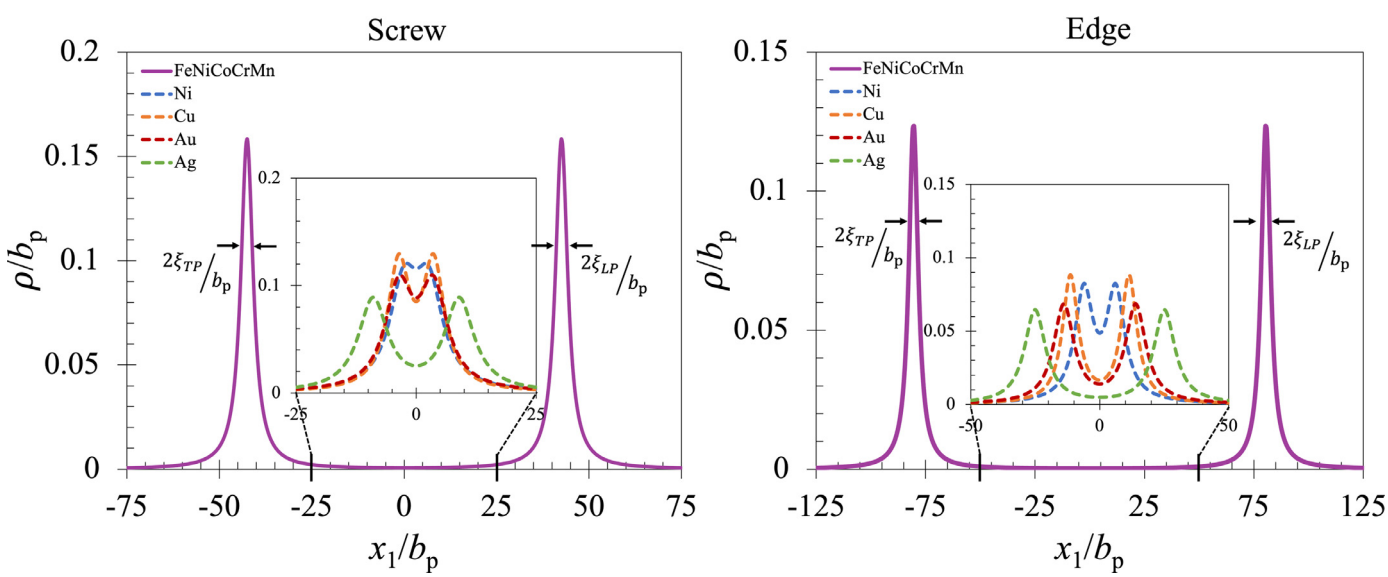

Fig. 11. Plot of the dislocation-density distributions corresponding to the energy-minimizing core-structure $(\xi^0_{TP}, \xi^0_{LP}, s^0_1, s^0_2)$ of the $a/2\langle 011\rangle$ extended dislocation, shown for both edge and screw characters of the dislocation.

following objective function:

$$E_{PATH}(C_0, C_1 \ldots, C_p) = \sum_{i=1}^{T_{\max}} E_{TOT}\left(s_1(t_i), s_2(t_i), \xi^0_{TP}, \xi^0_{TP}\right) \tag{29}$$

The path parameters that minimize E_{PATH} are determined using the unconstrained minimization routine *fminunc* in MATLAB®, and these parameters define the Minimum Energy Path (MEP). It is found that the MEP is not straight but has a wavy "zig-zag" nature, passing through the energetically-degenerate minima O, O_1 etc. (shown by the solid-line path in Fig. 12 (a)). The energy trajectory along the MEP is obtained from the landscape, and also compared to the trajectory along the straight path OO_1, shown in Fig. 12 (b). Clearly, the MEP exhibits a lower energy barrier for the

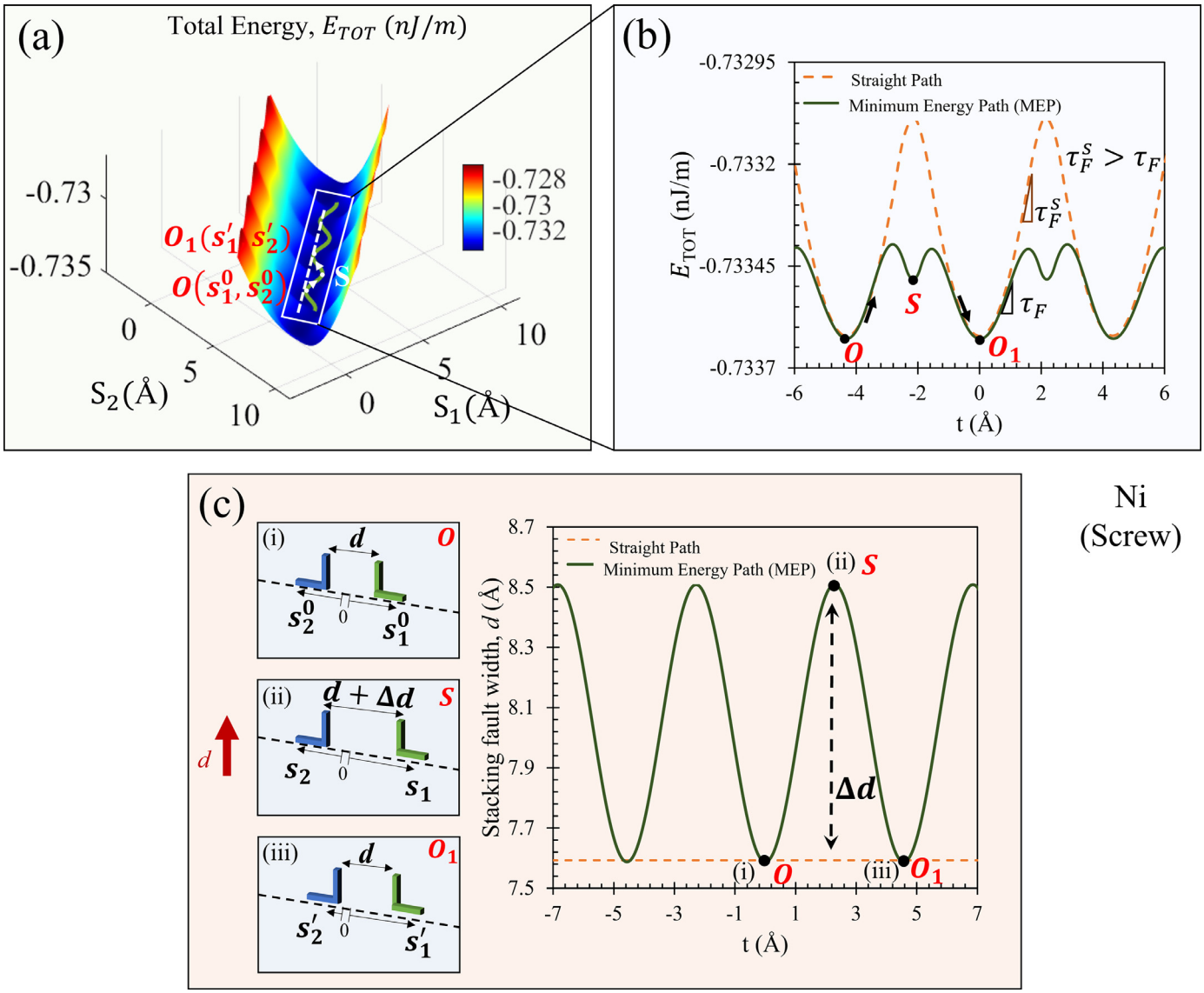

Fig. 12. Total-energy landscape of the $^a/_2\langle 011\rangle$ extended dislocation for a screw-dislocation in Ni (a) Plot of total-energy E_{TOT} against the position of the Shockley partials (s_1, s_2) indicating possible paths traversing across the energy minima $O = (s_1^0, s_2^0)$, $O_1 = (s'_1, s'_2)$; the dashed-line represents a straight-path in which the partials move together such that stacking-fault width between them is conserved i.e. $s_1 + s_2 = C$, is constant; the solid-line represents a zig-zag Minimum-Energy Path (MEP) where the partials don't move together and move intermittently, passing through an intermediate transition state S (b) Energy trajectories along the straight-path shown in (a), and the Minimum Energy Path (MEP); the energy barriers along the MEP are significantly lower indicating that the zig-zag nature of motion is preferred; the maximum gradient of the energy trajectories yields the CRSS for the MEP and the straight path, given by τ_F and τ_F^S respectively (elaborated in main text) (c) Schematic representation of the motion of the partials along the MEP, in which the leading partial (i) moves first, (ii) increases the fault-width from d to $d + \Delta d$ and then (iii) the trailing partial follows; a plot of the variation of the stacking-fault width during the motion is also given.

path of the dislocation, and also exhibits an intermediate stable transition state S. The variation of the stacking-fault width $d(t) = s_1(t) + s_2(t)$ is also determined and plotted in Fig. 12(c) showing how the fault-width does not remain constant but fluctuates during the motion of the dislocation. Fig. 13 shows the MEP determination for the case of $^a/_2\langle 011\rangle$ edge-dislocation in Ni, and it is observed that the path is nearly straight with minor zig-zag behavior. Thus, in addition to the non-straight MEP revealed by the approach, it is also revealed that the nature of motion of the dislocation can change with its character.

The final critical step is to determine the CRSS. Till date, the conventional Peierls-Nabarro approach has been adopted where the CRSS is given by the equation:

$$\tau_{CRSS}^{1D} = \max\left(\frac{1}{b_F}\frac{dE_{PN}^{SC-M}(\delta)}{d\delta}\right) \tag{30}$$

where $E_{PN}^{SC-M}(\delta) = \sum_{m=-\infty}^{\infty} \gamma(f(ma' - \delta))a'$, for γ defined in Eq. (20) and f by Eq. (3), motivated by the conventional SC-M misfit-energy model discussed in Section 2.2.2 (also refer Eq. (23)). There are multiple challenges in adopting this approach for the case of the $^a/_2\langle 011\rangle$ extended dislocation. For instance, (i) the path of the individual Shockley partials is ignored in this approach, (ii) the model presumes dependence on the total Burgers vector b_F alone and seemingly has no dependence on the partial Burgers vector b_P and (iii) Only the misfit-energy landscape is considered and in the one-dimensional form.

In this study, a novel approach is proposed in which the CRSS is determined from the energy-trajectory corresponding to the zig-zag MEP path on the total-energy landscape, advancing on all aforementioned fronts. The proposed approach is thus named the Optimum-Energy-Trajectory (OET) approach for CRSS prediction for FCC materials. Suppose the $^a/_2\langle 011\rangle$ extended dislocation is subject

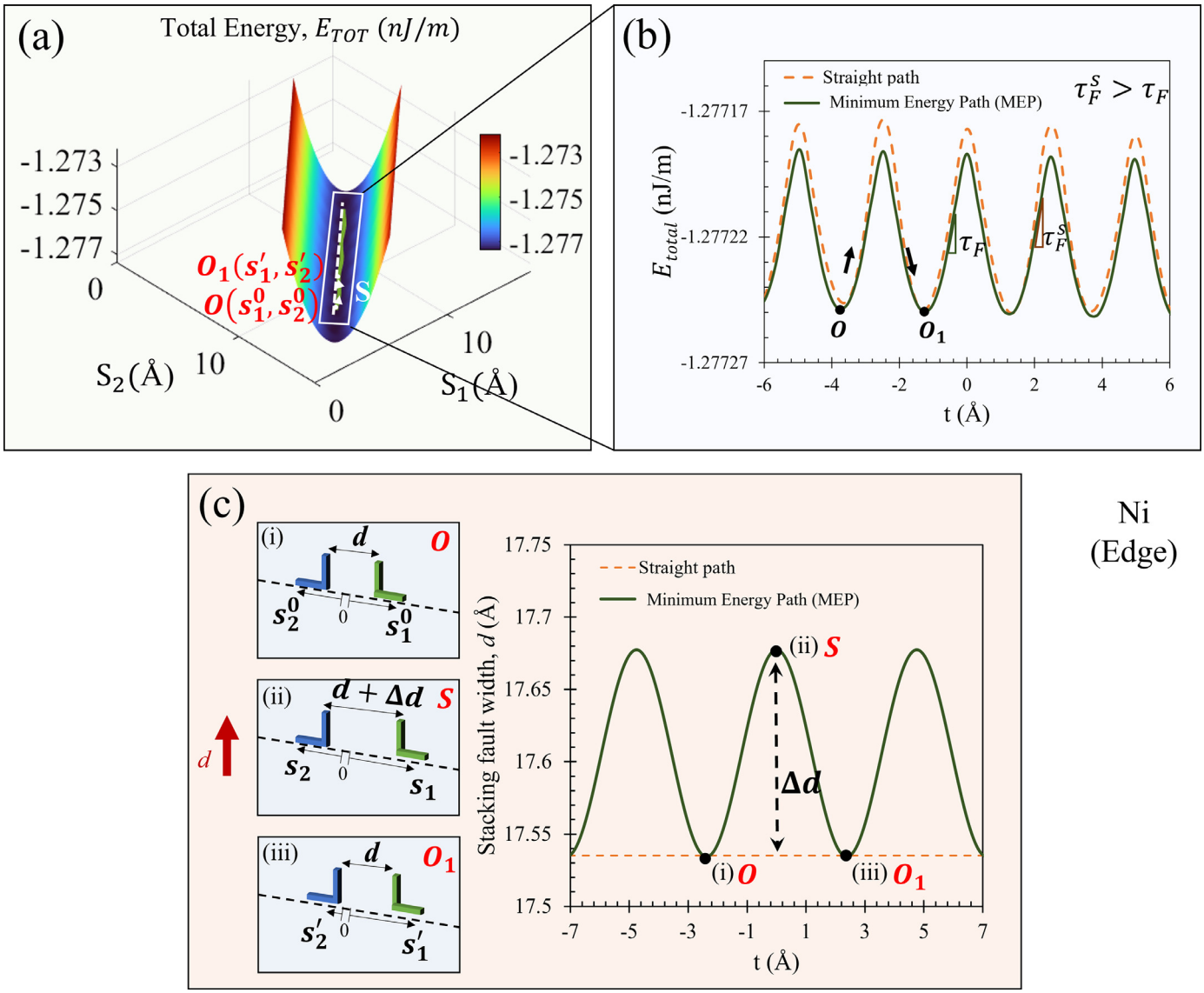

Fig. 13. Total-energy landscape of the $^a/_2\langle 011\rangle$ extended dislocation for a edge-dislocation in Ni (a) Plot of total-energy E_{TOT} against the position of the Shockley partials (s_1, s_2) indicating possible paths traversing across the energy minima $O(s^0_1, s^0_2)$, $O_1(s'_1, s'_2)$; the dashed-line represents a straight-path in which the partials move together such that stacking-fault width between them is conserved i.e. $s_1 + s_2 = C$, is constant; the solid-line represents a zig-zag Minimum-Energy Path (MEP) where the partials don't move together and move intermittently, passing through an intermediate transition state S (b) Energy trajectories along the straight-path shown in (a), and the Minimum Energy Path (MEP); the energy barriers along the MEP are significantly lower indicating that the zig-zag nature of motion is preferred; the maximum gradient of the energy trajectories yields the CRSS for the MEP and the straight path, given by τ_F and τ_F^S respectively (elaborated in main text) (c) Schematic representation of the motion of the partials along the MEP, in which the leading partial (i) moves first, (ii) increases the fault-width from d to $d + \Delta d$ and then (iii) the trailing partial follows; a plot of the variation of the stacking-fault width during the motion is also given.

to the stress-tensor $\underline{\underline{\sigma_a}}$. The applied load is considered to be a uniaxial tensile load along the $\hat{\nu}||[1\bar{3}2]$ direction, consequently given by $\underline{\underline{\sigma_a}} = \sigma_a(\hat{\nu} \otimes \hat{\nu})$. This direction of loading was chosen so as to result in the same Schmid factor for the trailing and leading Shockley partial. For motion of the dislocation, the change in Gibbs' free energy, dG, of the system must be considered, given by the equation:

$$dG = dE_{TOT} - dW \tag{31}$$

where dE_{TOT} is the change in the total-energy of the system and dW is the change in the work-interaction energy with motion of the dislocation. This is given by:

$$\begin{aligned} dW &= \left(\left(\underline{\underline{\sigma_a}}\hat{n}_{slip}\right).\vec{b}_{LP}\right)ds_1 + \left(\left(\underline{\underline{\sigma_a}}\hat{n}_{slip}\right).\vec{b}_{TP}\right)(-ds_2) \\ &= \sigma_a b_p(SF_{LP}ds_1 + SF_{TP}(-ds_2)) \\ &= \sigma_a b_p\left(SF_{LP}s'_1(t) - SF_{TP}s'_2(t)\right)dt \end{aligned} \tag{32}$$

where $\hat{n}_{slip} = {}^1/_{\sqrt{3}}[1\bar{1}1]$ is the normal to the slip-plane, ds_1 and ds_2 respectively represent the change in the positions of the leading and trailing partials respectively, SF_{LP} and SF_{TP} are the Schmid factors corresponding to the leading and trailing partials respectively, and $s_1(t)$, $s_2(t)$ parametrize the MEP. The Schmid factors are given by the equations $SF_{LP} = (\hat{\nu} \cdot \hat{n}_{slip})(\hat{\nu} \cdot \hat{b}_{LP})$ and$SF_{TP} = (\hat{\nu} \cdot \hat{n}_{slip})(\hat{\nu} \cdot \hat{b}_{TP})$, where $\hat{b}_{TP}$ and $\hat{b}_{LP}$ are unit vectors along the Burgers vectors of the trailing and leading partials respectively. The negative sign attached to the $s'_2(t)$ term on the RHS is because s_2 and s_1 are defined in opposite sense to each other (refer Fig. 2(a)). At the onset of motion, the condition $dG = 0$ is achieved. With this condition, and from Eqs. (32) and (31), it follows that the critical applied stress for motion is given by:

$$\sigma_a^{cr.} = \max\left(\frac{1}{(SF_{LP}s'_1(t) - SF_{TP}s'_2(t))}\left(\frac{1}{b_p}\frac{dE_{TOT}}{dt}\right)\right) \tag{33}$$

Table 4
Comparison of proposed analytical framework in this study against experiment and a commonly employed exponential model# of CRSS.

Material	Exponential CRSS model{ξ_{ISO}(Å), $\tau_F^{expo.}$(MPa)}	CRSS model of this Study{ξ_{LP}(Å), τ_F(MPa)}(Eq. (34))	Experiment τ_F(MPa)
Ni	{1.47, **2539.8**}	{4.29, **8.6**}	**4.7–9** [65,66]
Cu	{1.60, **1310.8**}	{3.70, **2.1**}	**0.5–3.2** [65,67–69]
Au	{2.01, **555.2**}	{4.78, **1.4**}	**0.9** [70]
Ag	{1.91, **650.9**}	{4.98, **1.3**}	**0.3–0.7** [46,65]
FeNiCoCrMn	{1.04, **6469.0**}	{2.01, **147.4**}	**135–172** [71,72]

The critical applied stress is resolved along the slip-system of the extended dislocation to determine the critical stress in the resolved form, yielding the CRSS as:

$$\tau_F = \sigma_a^{cr.} SF_{FULL} = SF_{FULL}.\max\left(\frac{1}{\left(SF_{LP}s'_1(t) - SF_{TP}s'_2(t)\right)}\left(\frac{1}{b_p}\frac{dE_{TOT}}{dt}\right)\right) \quad (34)$$

where $SF_{FULL} = (\hat{\nu}\cdot\hat{n}_{slip})(\hat{\nu}\cdot\hat{b}_F)$ is the Schmid factor for the full extended dislocation on its slip system, with $\hat{b}_F$ representing the unit vector along the direction of the Burgers vector $\vec{b}_F$. Figs. 12 (b) and 13 (b) show the comparison between the computed CRSS corresponding to a straight-path and the MEP, given by τ_F^S and τ_F respectively. It is observed that $\tau_F < \tau_F^S$, establishing the CRSS to be equal to τ_F corresponding to the MEP path. This is expected since the energy barriers and gradients along the MEP are both lower than the straight path. Thus, the CRSS for the $a/2\langle 011\rangle$ has been determined.

Finally, the efficacy of the model is validated by comparing against a benchmark exponential relation commonly employed for predicting the CRSS [59–64] and by comparison with available experimental data. This comparison is presented in Table 4. The proposed framework significantly improves on the benchmark model by yielding CRSS predictions of the correct order, agreeing well with experiments. Predictions of the framework are also compared with another popular approach that determines the core-width based on the shear strength $\tau_{\max}$ and an alternately-defined anisotropic factor K, subsequently applying the exponential model for CRSS [31,45]. Comparisons are shown in table A1 of Appendix A yet again noting the significant improvement offered by the proposed framework.

$\#\tau_F^{expo.} = (G/A_\nu)\exp(-2\pi\xi_{iso.}/b_F)$, employing the isotropic core-width $\xi_{ISO} = d_{\{111\}}/2A_\nu$, where $A_\nu = 1-\nu$ for edge-character dislocation and $A_\nu = 1$ for screw-character dislocation, G is the isotropic shear modulus and ν is the Poisson's ratio, listed in table A2 in Appendix A

3. Discussions

The current study proposes a predictive analytical framework for the CRSS of $a/2\langle 011\rangle$ extended dislocations in FCC materials. The proposed framework determines the core-parameters of the dislocation without any apriori assumptions and predicts the CRSS from these parameters for extended dislocations in FCC materials. The core-parameters, namely the core-widths of the Shockley partials (ξ_{TP} and ξ_{LP}) and their positions (s_1 and s_2), are determined by a minimization of the total energy of the dislocation. Existing approaches have thus far involved assumptions or some form of empiricism associated with the calculation of the core-widths and in the formulations for the continuum strain energy or the atomistic misfit energy. For instance, several works employ the isotropic formulae for core-widths ($\xi_{EDGE} = d_{\{111\}}/(2(1-\nu))$ for edge character or $\xi_{SCREW} = d_{\{111\}}/2$ for screw character, where $d_{\{111\}}$ is the interplanar spacing between consecutive {111} planes and ν is the Poisson's ratio) even for anisotropic materials. Additionally, in calculation of the strain-energy, either isotropy is inherently assumed or an ad-hoc correctional-factor for anisotropy is employed (represented by K) in the calculation of the core-width. In calculation of the misfit energy, the choice of a' as the discrete lattice parameter separating rows of atoms (in the conventional SC-M approach) is inconsistent with the underlying crystal structure of the slip plane. Furthermore, idealized limits of "narrow" or "wide" core-widths are commonly employed to afford use of simpler analytical expressions for the core-width and the CRSS [46], without accurate basis for whether the core-widths in the material are at either limit in reality. The proposed formalism eliminates all such empiricism or assumptions and determines the core-parameters.

The current study offers multiple advancements in prediction of the continuum strain-energy and atomistic misfit-energy of the extended dislocation. A fully-anisotropic calculation of the strain-energy is proposed employing the Eshelby-Stroh (E-S) formalism, determining the anisotropic interaction coefficients, K_{ij} $(i, j = 1, 2)$ directly from the E-S strain-fields and strain-energies. Such an approach is particularly critical to evaluate the strain-energies of interactions between the $a/6\langle 112\rangle$ Shockley partials, which are generally of mixed character even for a pure-edge or pure-screw character of the $a/2\langle 011\rangle$ extended dislocation, as considered in this study. The proposed WS-M model offers a significant and necessary advancement over the current SC-M understanding of misfit-energy within the core of the dislocation. The proposed approach offers a framework which, for the first time, accommodates the complete crystal structure on the slip plane. It is shown that the conventional SC-M approach of representing the crystal structure as rows of atoms separated a'-distance apart is inaccurate. The correct atomic-positions have a two-dimensionality which can only be captured by a two-lattice-vector $\vec{a}_1 - \vec{a}_2$ basis as done in this study, and the spacing between the atomic-rows is not equal to the conventional choice of a' that has so far been adopted (refer Fig. 6). Furthermore, at each atomic-site, a Wigner-Seitz (W-S) cell area is defined which provides a physically-motivated discrete domain assigned to each site and partitions the crystal structure around the core into 3D-cells of disregistry, the fault-energies within which are exactly those that the GSFE simulation delivers (refer Section 2.2.2 and Fig. 7). The WS-M approach is also capable of handling mixed dislocation character (for the $a/2\langle 011\rangle$ dislocation and/or its partials) since the lattice-vectors $\vec{a}_1 - \vec{a}_2$ can be accordingly defined depending on the relative orientation of the slip-plane crystal structure with respect to the dislocation-line direction. Each of these advancements offers sufficient physical fidelity to reliably model the core-structures of dislocations in other crystal structures such as Hexagonally-Closed Packed (HCP) materials. It can further be adapted for dislocations at interfaces of anisotropic media, allowing determination of core-structures and CRSS predictions for interface dislocations such on twin boundaries [73,74] or film-substrate interfaces [75]. Also from a conceptual standpoint, it would be a promising direction for future research to analyze the impact of individual advancements in this framework, for instance of (a) elastic anisotropy by comparing the CRSS predictions with isotropic values of the interaction coefficient K against the anisotropically computed coefficient and (b) the misfit-

energy model, comparing the predictions from SC-M and WS-M models.

The proposed framework deals with all core-parameters $(\xi_{TP}, \xi_{LP}, s_1, s_2)$ in a coupled manner, allowing the framework to capture a wide variety of core-structures, both narrow and wide. For instance, as seen in Fig. 11, the approach predicts core-structures of $^a/_2\langle 011\rangle$-screw dislocations in Ni which spans a width along x_1 that is about 15x smaller than that of the HEA FeNiCoCrMn. Modeling such a range of cores, particularly in the narrow end, requires the model to capture the coupled-influence of both the unstable stacking fault energy barrier γ_{us} and the stable stacking fault energy barrier γ_{isf} as both can dictate the core-widths and the fault-width. This is unlike most treatments till date that treat the stacking fault width disjoint from the core-widths, thought to be respectively dependent on γ_{isf} and γ_{us} in a disjoint manner, and thus only capable of reliably modeling a well-dissociated dislocation (i.e. sufficiently large fault-width).

The current approach establishes the contrasting trends in the continuum strain-energy and the atomistic misfit-energy with respect to the core-parameters $(\xi_{TP}, \xi_{LP}, s_1, s_2)$ (refer Section 2.2.3, Figs. 9 and 10). The existence of a total-energy minimum at $(\xi^0_{TP}, \xi^0_{LP}, s^0_1, s^0_2)$ is illustrated and the existence of multiple energetically-degenerate minima on the total-energy landscape, E_{TOT}, is also revealed. Knowledge of the energy-landscape to such detail is necessary to know the nature of motion undertaken by the dislocation under applied stress. In considering the $^a/_2\langle 011\rangle$ extended dislocation, it can often be a tacit assumption that dislocation motion occurs by simultaneous motion of its partials, preserving the fault-width in between. This study shows for the first time that such motion is energetically unfavorable as it would encounter a higher energy barrier. The existence of Minimum-Energy-Path (MEP) on the energy-landscape is proposed and solved for, establishing the motion of the extended dislocation to occur in a "zig-zag" manner through intermittent motion of its individual partials. And it is this MEP that has led to the accurate prediction of the CRSS of the $^a/_2\langle 011\rangle$ extended dislocation.

A novel Optimum-Energy-Trajectory (OET) approach to predict the CRSS of $^a/_2\langle 011\rangle$ extended dislocations is proposed advancing over the conventional Peierls-Nabarro framework. The proposed method is grounded in first-principles energetics and reveals the dependence of the CRSS on three Schmid factors – the Schmid factor of the $^a/_2\langle 011\rangle$ dislocation, SF_{FULL} and that corresponding to each partial, SF_{TP} and SF_{LP}. Dependencies of the CRSS on the gradients of the total-energy landscape $^{dE_{TOT}}/_{dt}$ along the MEP, and the gradient of motion of the individual partials, $s'_1(t)$ and $s'_2(t)$, are clearly revealed for the first time in literature. The model reveals why it is insufficient to consider the full Schmid factor SF_{FULL} alone since the motion of the extended dislocation is mediated by its individual partials. Further, the proposed framework is capable of predicting the CRSS in the presence of an external stress causing unequal Schmid factors, $SF_{TP} \neq SF_{LP}$, where the motion of one partial is more preferred than the other. Dependencies on the character of the dislocation, elastic anisotropy and the underlying crystal structure are captured by the total-energy landscape E_{TOT}, ultimately influencing the MEP and the corresponding gradients $^{dE_{TOT}}/_{dt}$. To the best of the authors' knowledge, the proposed framework is the first one in literature capable of accounting of all the aforementioned effects involved in the motion of the extended dislocation. The efficacy of the predictions is illustrated by the agreement with experimental results in Table 4, advancing over a commonly employed exponential model for the CRSS.

4. Conclusions

The current study proposes a predictive analytical framework for the core-widths and CRSS of $^a/_2\langle 011\rangle$ extended dislocation in Face-Centered-Cubic (FCC) materials, without involving any empiricism. The following advancements are offered:

a The proposed framework accounts for the full elastic anisotropy in the material and the fault energies on the slip plane, predicting the core-width from an optimal balance between the continuum strain-energies and atomistic-misfit energies.
b A methodology to determine the anisotropic interaction coefficients K_{ij} directly from the Eshelby-Stroh strain-fields around dislocations is proposed leading to accurate calculation of the strain-energy of interaction for arbitrary material anisotropy.
c A novel Wigner-Seitz-Cell-Misfit (WS-M) energy model is proposed to predict the core-misfit energy through incorporation of the correct atomic positions on the slip-plane crystal structure and the correct planar-domain (ΔA– Wigner-Seitz cell area) around each site over which the local fault-energy of disregistry is prevalent.
d A robust procedure to determine the core-parameters for the extended dislocation is proposed, determining both the core-widths of the Shockley partials and the stacking fault width simultaneously. This approach allows modeling dislocations whose cores can either be well-dissociated with large fault width (e.g. FeNiCoCrMn) or on the other extreme, narrow cores with such small width that the partial cores exhibit overlap (e.g. Ni).
e The nature of motion of the extended dislocation is revealed by determining the Minimum-Energy-Path (MEP) of motion across the total-energy landscape. The MEP reveals a zig-zag nature of motion involving intermittent motion of the individual Shockley partials challenging the common notion that the partials move together. The zig-zag motion allows for a fluctuating stacking fault-width during motion of the extended dislocation.
f A novel Optimum-Energy-Trajectory (OET) approach to predict the CRSS of extended dislocations is proposed, grounded in first-principles energetics and incorporating the determined MEP of the dislocation. Dependencies on the total-energy gradient along the MEP, along with the gradients of motion of the individual partials and their Schmid factors are clearly established, developing a new analytical expression for the CRSS advancing over the state-of-the-art understanding in the field.
g The proposed framework is validated by comparison with available experimental data and the advancement offered by the framework is established by comparison against a popular benchmark exponential relation.

Thus, this study proposes a fully predictive model for dislocation slip in FCC materials, significantly advancing over the state-of-the-art models and addressing a major void in structure-property prediction for structural materials, now capable of being employed for design/exploration of material compositions with unprecedented yield strength.

Declaration of Competing Interest

The authors declare that they have no known competing financial interests or personal relationships that could have appeared to influence the work reported in this paper.

Acknowledgments

We note that A. S. K. Mohammed and O. K. Celebi contributed equally to this paper. The work is supported by the National Science Foundation (NSF) under award number 2125821 and partly by the Air Force Office of Scientific Research (AFOSR) under award number FA9550–18–1–0198, which is gratefully acknowledged. The use of the Illinois Campus Cluster, a computing resource that is

operated by the Illinois Campus Cluster Program (ICCP) in conjunction with the National Center for Supercomputing Applications (NCSA) and which is supported by funds from the University of Illinois at Urbana-Champaign, is also gratefully acknowledged.

Appendix A: Comparison of predictions from proposed models against existing models

Table A1: Comparison of proposed analytical framework in this study against alternate prior model for core-width prediction and CRSS

Material	Exponential model for CRSS based on core-width calculated through K-factor and shear strength τ_{max}[46]				Proposed Approach in this study	
	τ_{max} (GPa)	K (GPa)	$\xi_K = Kb_F/4\pi\tau_{max}$ (Å)	$\tau_F^{expo.-K}$ (MPa)	ξ_{LP} (Å)	τ_F (MPa)
Cu	1.8 [46]	69.2	7.8	3×10^{-4}	3.70	2.1
Ag	0.89 [46]	45.9	12.07	2×10^{-7}	4.78	1.4
FeNiCoCrMn	4.4 [45]	149	6.86	5×10^{-3}	2.01	147.4

#$\tau_F^{expo.-K} = (G/A_\nu)\exp(-2\pi\xi_K/b_F)$, employing $\xi_K = Kb_F/(4\pi\tau_{max})$, $A_\nu = 1-\nu$ for edge-character dislocation and $A_\nu = 1$ for screw-character dislocation, G is the isotropic shear modulus and ν is the Poisson's ratio, listed in table A2

Table A2: Isotropic shear modulus G and Poisson's ratio ν for materials considered in this study (employed in calculations of Tables 3 and A1)

Material	G (GPa)	ν
Ni	76 [76]	0.31 [76]
Cu	45 [76]	0.35 [76]
Au	27.6 [76]	0.42 [76]
Ag	28.9 [76]	0.37 [76]
FeNiCoCrMn	80 [77]	0.26 [77]

References

[1] F. Brenne, A.S.K. Mohammed, H. Sehitoglu, High resolution atomic scale characterization of dislocations in high entropy alloys: critical assessment of template matching and geometric phase analysis, Ultramicroscopy 219 (2020) 113134.
[2] A.S.K. Mohammed, H. Sehitoglu, Martensitic twin boundary migration as a source of irreversible slip in shape memory alloys, Acta Mater. 186 (2020) 50–67.
[3] W.G. Nöhring, W.A. Curtin, Design using randomness: a new dimension for metallurgy, Scr. Mater. 187 (2020) 210–215.
[4] W. Li, S. Chen, P.K. Liaw, Discovery and design of fatigue-resistant high-entropy alloys, Scr. Mater. 187 (2020) 68–75.
[5] J.H. Panchal, S.R. Kalidindi, D.L. McDowell, Key computational modeling issues in Integrated Computational Materials Engineering, Comput. Aided Des. 45 (1) (2013) 4–25.
[6] R.O. Ritchie, Toughening materials: enhancing resistance to fracture, Philos. Trans. R. Soc., A 379 (2203) (2021) 20200437.
[7] G. Gengor, A.S.K. Mohammed, H. Sehitoglu, {101¯2} Twin interface structure and energetics in HCP materials, Acta Mater. 219 (2021) 117256.
[8] R. Sidharth, A.S.K. Mohammed, W. Abuzaid, H. Sehitoglu, Unraveling frequency effects in shape memory alloys: NiTi and FeMnAlNi, Shape Memory and Superelasticity 7 (2) (2021) 235–249.
[9] R. Peierls, The size of a dislocation, Proc. Phys. Soc. 52 (1) (1940) 34–37.
[10] J.P. Hirth, J. Lothe, Theory of dislocations, J. Appl. Mech. 50 (2) (1983) 476–477.
[11] F.R.N. Nabarro, Dislocations in a simple cubic lattice, Proceedings of the Physical Society 59(2) (1947) 256–272.
[12] S. Alkan, H. Sehitoglu, Dislocation core effects on slip response of NiTi- a key to understanding shape memory, Int. J. Plast. 97 (2017) 126–144.
[13] G. Liu, X. Cheng, J. Wang, K. Chen, Y. Shen, Peierls stress in face-centered-cubic metals predicted from an improved semi-discrete variation Peierls-Nabarro model, Scr. Mater. 120 (2016) 94–97.
[14] H.B. Huntington, Modification of the Peierls-Nabarro model for edge dislocation core, Proc. Phys. Soc. London Sect. B 68 (12) (1955) 1043–1048.
[15] K. Ohsawa, H. Koizumi, H.O.K. Kirchner, T. Suzuki, The critical stress in a discrete Peierls–Nabarro model, Philos. Mag. A 69 (1) (1994) 171–181.
[16] G. Schoeck, The generalized Peierls–Nabarro model, Philos. Mag. A 69 (6) (1994) 1085–1095.
[17] V.V. Bulatov, E. Kaxiras, Semidiscrete variational Peierls framework for dislocation core properties, Phys. Rev. Lett. 78 (22) (1997) 4221–4224.
[18] G. Schoeck, The Peierls dislocation: line energy, line tension, dissociation and deviation, Acta Mater. 45 (6) (1997) 2597–2605.
[19] J. Hartford, B. von Sydow, G. Wahnström, B.I. Lundqvist, Peierls barriers and stresses for edge dislocations in Pd and Al calculated from first principles, Phys. Rev. B 58 (5) (1998) 2487–2496.
[20] R. Miller, R. Phillips, G. Beltz, M. Ortiz, A non-local formulation of the peierls dislocation model, J. Mech. Phys. Solid. 46 (10) (1998) 1845–1867.
[21] B.v. Sydow, J. Hartford, G. Wahnström, Atomistic simulations and Peierls–Nabarro analysis of the Shockley partial dislocations in palladium, Comput. Mater. Sci. 15 (3) (1999) 367–379.
[22] W. Shaofeng, Lattice theory for structure of dislocations in a two-dimensional triangular crystal, Phys. Rev. B 65 (9) (2002) 094111.
[23] P. Szelestey, M. Patriarca, K. Kaski, Computational study of core structure and Peierls stress of dissociated dislocations in nickel, Model. Simul. Mater. Sci. Eng. 11 (6) (2003) 883–895.
[24] G. Schoeck, The Peierls model: progress and limitations, Mater. Sci. Eng. A 400-401 (2005) 7–17.
[25] V.A. Lubarda, X. Markenscoff, Variable core model and the Peierls stress for the mixed (screw-edge) dislocation, Appl. Phys. Lett. 89 (15) (2006) 151923.
[26] G. Schoeck, The core structure of dislocations: peierls model vs. atomic simulation, Acta Mater. 54 (18) (2006) 4865–4870.
[27] P. Carrez, D. Ferré, P. Cordier, Peierls–Nabarro model for dislocations in MgSiO3 post-perovskite calculated at 120 GPa from first principles, Philos. Mag. 87 (22) (2007) 3229–3247.
[28] C. Woodward, D.R. Trinkle, L.G. Hector, D.L. Olmsted, Prediction of dislocation cores in aluminum from density functional theory, Phys. Rev. Lett. 100 (4) (2008) 045507.
[29] Y. Xiang, H. Wei, P. Ming, W. E, A generalized Peierls–Nabarro model for curved dislocations and core structures of dislocation loops in Al and Cu, Acta Mater. 56 (7) (2008) 1447–1460.
[30] E. Clouet, L. Ventelon, F. Willaime, Dislocation core energies and core fields from first principles, Phys. Rev. Lett. 102 (5) (2009) 55502-55502.
[31] D.C. Chrzan, M.P. Sherburne, Y. Hanlumyuang, T. Li, J.W. Morris, Spreading of dislocation cores in elastically anisotropic body-centered-cubic materials: the case of gum metal, Phys. Rev. B 82 (18) (2010) 184202-184202.
[32] I.J. Beyerlein, A. Hunter, Understanding dislocation mechanics at the mesoscale using phase field dislocation dynamics, Philos. Trans. R. Soc., A 374 (2066) (2016) 20150166.
[33] G. Liu, X. Cheng, J. Wang, K. Chen, Y. Shen, Improvement of nonlocal Peierls-Nabarro models, Comput. Mater. Sci. 131 (2017) 69–77.
[34] M. Poschmann, M. Asta, D.C. Chrzan, Convergence of calculated dislocation core structures in hexagonal close packed titanium, Model. Simul. Mater. Sci. Eng. 26 (1) (2017) 014003.
[35] D. Rodney, L. Ventelon, E. Clouet, L. Pizzagalli, F. Willaime, Ab initio modeling of dislocation core properties in metals and semiconductors, Acta Mater. 124 (2017) 633–659.
[36] B.A. Szajewski, A. Hunter, I.J. Beyerlein, The core structure and recombination energy of a copper screw dislocation: a Peierls study, Philos. Mag. 97 (25) (2017) 2143–2163.
[37] M. Boleininger, T.D. Swinburne, S.L. Dudarev, Atomistic-to-continuum description of edge dislocation core: unification of the Peierls-Nabarro model with linear elasticity, Phys. Rev. Mater. 2 (8) (2018).
[38] Y. Kamimura, K. Edagawa, A.M. Iskandarov, M. Osawa, Y. Umeno, S. Takeuchi, Peierls stresses estimated via the Peierls-Nabarro model using ab-initio γ-surface and their comparison with experiments, Acta Mater. 148 (2018) 355–362.
[39] B.A. Szajewski, A. Hunter, D.J. Luscher, I.J. Beyerlein, The influence of anisotropy on the core structure of Shockley partial dislocations within FCC materials, Model. Simul. Mater. Sci. Eng. 26 (1) (2018) 015010.
[40] M. Boleininger, S.L. Dudarev, Continuum model for the core of a straight mixed dislocation, Phys. Rev. Mater. 3 (9) (2019) 093801.
[41] K. Edagawa, Y. Kamimura, A.M. Iskandarov, Y. Umeno, S. Takeuchi, Peierls stresses estimated by a discretized Peierls–Nabarro model for a variety of crystals, Materialia 5 (2019) 100218.
[42] X. Liu, Z. Pei, M. Eisenbach, Dislocation core structures and Peierls stresses of the high-entropy alloy NiCoFeCrMn and its subsystems, Mater. Des. 180 (2019) 107955.
[43] X. Hu, S. Wang, Nonplanar core structure of the screw dislocations in tantalum from the improved Peierls–Nabarro theory, Philos. Mag. 98 (6) (2018) 484–516.
[44] B.A. Szajewski, A. Hunter, D.J. Luscher, Analytic model of the γ-surface deviation and influence on the stacking fault width between partial dislocations, Comput. Mater. Sci. 147 (2018) 243–250.
[45] X. Li, S. Schönecker, W. Li, L.K. Varga, D.L. Irving, L. Vitos, Tensile and shear loading of four fcc high-entropy alloys: a first-principles study, Phys. Rev. B 97 (9) (2018) 94102-94102.
[46] B. Joós, M.S. Duesbery, The Peierls Stress of Dislocations: an Analytic Formula, Phys. Rev. Lett. 78 (2) (1997) 266–269.
[47] A.H.W. Ngan, A generalized Peierls-Nabarro model for nonplanar screw dislocation cores, J. Mech. Phys. Solid. 45 (6) (1997) 903–921.
[48] D.M. Barnett, J. Lothe, An image force theorem for dislocations in anisotropic bicrystals, J. Phys. F Met. Phys. 4 (10) (1974) 1618–1635.
[49] A.N. Stroh, Dislocations and cracks in anisotropic elasticity, Philos. Mag. 3 (30) (1958) 625–646.
[50] S. Gene, W. Herbert, Single Crystal Elastic Constants and Calculated Aggregate Properties, Cambridge, MA: MIT1971.

[51] J.R. Neighbours, C.S. Smith, The elastic constants of copper alloys, Acta Metall. 2 (4) (1954) 591–596.
[52] S. Alkan, A. Ojha, H. Sehitoglu, Determination of latent hardening response for FeNiCoCrMn for twin-twin interactions, Acta Mater. 147 (2018) 149–164.
[53] S. Kibey, J.B. Liu, M.J. Curtis, D.D. Johnson, H. Sehitoglu, Effect of nitrogen on generalized stacking fault energy and stacking fault widths in high nitrogen steels, Acta Mater. 54 (11) (2006) 2991–3001.
[54] O.K. Celebi, A.S.K. Mohammed, J.A. Krogstad, H. Sehitoglu, Evolving dislocation cores at Twin Boundaries: theory of CRSS elevation, Int. J. Plast. 148 (2022) 103141.
[55] S. Kibey, J.B. Liu, D.D. Johnson, H. Sehitoglu, Predicting twinning stress in fcc metals: linking twin-energy pathways to twin nucleation, Acta Mater. 55 (20) (2007) 6843–6851.
[56] Y. Shen, X. Cheng, Dislocation movement over the Peierls barrier in the semi-discrete variational Peierls framework, Scr. Mater. 61 (5) (2009) 457–460.
[57] H. Yu, S. Cao, S.S. Youssef, Y.-.J. Ma, J.-.F. Lei, Y. Qi, Q.-.M. Hu, R. Yang, Generalized stacking fault energies and critical resolved shear stresses of random α-Ti-Al alloys from first-principles calculations, J. Alloys Compd. 850 (2021) 156314.
[58] C. Giacovazzo, Symmetry in crystals, Fundamentals of Crystallography, Oxford University Press, Oxford, 2011.
[59] D. Qiu, P. Zhao, D.R. Trinkle, Y. Wang, Stress-dependent dislocation core structures leading to non-Schmid behavior, Mater. Res. Lett. 9 (3) (2021) 134–140.
[60] Y.Y. Zhao, T.G. Nieh, Correlation between lattice distortion and friction stress in Ni-based equiatomic alloys, Intermetallics 86 (2017) 45–50.
[61] H. Huang, X. Li, Z. Dong, W. Li, S. Huang, D. Meng, X. Lai, T. Liu, S. Zhu, L. Vitos, Critical stress for twinning nucleation in CrCoNi-based medium and high entropy alloys, Acta Mater. 149 (2018) 388–396.
[62] Z. Wang, Q. Fang, J. Li, B. Liu, Y. Liu, Effect of lattice distortion on solid solution strengthening of BCC high-entropy alloys, J. Mater. Sci. Technol. 34 (2) (2018) 349–354.
[63] S.S. Sohn, A. Kwiatkowski da Silva, Y. Ikeda, F. Körmann, W. Lu, W.S. Choi, B. Gault, D. Ponge, J. Neugebauer, D. Raabe, Ultrastrong medium-entropy single-phase alloys designed via severe lattice distortion, Adv. Mater. 31 (8) (2019) 1807142.
[64] D. Wei, X. Li, S. Schönecker, J. Jiang, W.-.M. Choi, B.-.J. Lee, H.S. Kim, A. Chiba, H. Kato, Development of strong and ductile metastable face-centered cubic single-phase high-entropy alloys, Acta Mater. 181 (2019) 318–330.
[65] J.N. Wang, Prediction of Peierls stresses for different crystals, Mater. Sci. Eng. A 206 (2) (1996) 259–269.
[66] P.S. Venkatesan, D.N. Beshers, Internal Friction Studies in Nickel Crystals from 77° to 298°K, J. Appl. Phys. 41 (1) (1970) 42–49.
[67] M.A. Adams, A.H. Cottrell, CXXXI, Effect of temperature on the flow stress of work-hardened copper crystals, Lond. Edinbur. Dubl. Philos. Mag. J. Sci. 46 (382) (1955) 1187–1193.
[68] P.J. Jackson, Z.S. Basinski, Latent hardening and the flow stress in copper single crystals, Can. J. Phys. 45 (2) (1967) 707–735.
[69] T.H. Blewitt, R.R. Coltman, J.K. Redman, Low-temperature deformation of copper single crystals, J. Appl. Phys. 28 (6) (1957) 651–660.
[70] Y. Kamimura, K. Edagawa, S. Takeuchi, Experimental evaluation of the Peierls stresses in a variety of crystals and their relation to the crystal structure, Acta Mater. 61 (1) (2013) 294–309.
[71] W. Abuzaid, H. Sehitoglu, Critical resolved shear stress for slip and twin nucleation in single crystalline FeNiCoCrMn high entropy alloy, Mater. Charact. 129 (2017) 288–299.
[72] E.P. George, W.A. Curtin, C.C. Tasan, High entropy alloys: a focused review of mechanical properties and deformation mechanisms, Acta Mater. 188 (2020) 435–474.
[73] A.S.K. Mohammed, H. Sehitoglu, Modeling the interface structure of type II twin boundary in B19′ NiTi from an atomistic and topological standpoint, Acta Mater. 183 (2020) 93–109.
[74] A.S.K. Mohammed, H. Sehitoglu, Strain-sensitive topological evolution of twin interfaces, Acta Mater. 208 (2021) 116716.
[75] C.-.L. Lee, S. Li, A half-space Peierls–Nabarro model and the mobility of screw dislocations in a thin film, Acta Mater. 55 (6) (2007) 2149–2157.
[76] W. Köster, H. Franz, Poisson's ratio for metals and alloys, Metallur. Rev. 6 (1) (1961) 1–56.
[77] Z. Wu, H. Bei, G.M. Pharr, E.P. George, Temperature dependence of the mechanical properties of equiatomic solid solution alloys with face-centered cubic crystal structures, Acta Mater. 81 (2014) 428–441.